Megadunes in Antarctica: migration and ~~evolution~~characterization from remote and in situ observations

Giacomo Traversa[1, 2], Davide Fugazza[2] and Massimo Frezzotti[3]

[1] Department of Physical Sciences, Earth and Environment (DSFTA), Università degli Studi di Siena, 53100 Siena, Italy
[2] Department of Environmental Science and Policy (ESP), Università degli Studi di Milano, 20133 Milan, Italy
[3] Department of Science, Università degli Studi Roma Tre, 00146 Rome, Italy

Correspondence to: Giacomo Traversa (~~giacomo.traversa@student.unisi.it~~giacomo.traversa@student.unisi.it) and Massimo Frezzotti (massimo.frezzotti@uniroma3.it)

Abstract. Megadunes are peculiar ~~snow dune fields~~features formed by the interaction between atmosphere and cryosphere and are known to be present only on the East Antarctic plateau and other planets (Mars and Pluto). ~~Antarctic megadunes are climatically important because their leeward flanks are characterized by glazed surfaces, a particular morphogenetic state of snow which makes these zones ablation areas, as their surface mass balance is near-zero or negative, on a continental ice sheet where surface mass balance is on average positive. This work builds on previous efforts in~~In this ~~field and by taking advantage from the most recent remote-sensing products and techniques coupled with field data, aims to provide new information and confirm previous hypotheses about megadunes. Focusing~~study, we have analysed the glaciological dynamic of megadunes, their spectral properties and morphology on two sample areas of the East Antarctic plateau where in the past international field activities were carried out (EAIIST and It-ITASE~~), we analysed the dynamic parameters of megadunes, their albedo and morphology. For the first time we provide a detailed analysis of their upwind migration, in all its components (absolute, sedimentological and ice flow) from remote and field observations, finding absolute values of approximately 10 m a^{-1} and demonstrating the upwind migration of dune windward flanks, with a relative stability of the leeward faces.~~). Using ~~remote sensing~~satellite images spanning 7 years, we analysed ~~their optical~~ the spatial and temporal variability of megadune surface characteristics, i.e., ~~albedo (broadband and~~ near infrared (NIR~~),~~) albedo, thermal brightness temperature and ~~topographic parameters, including slope, aspect and slope~~ Slope along the ~~prevailing wind direction~~Prevailing Wind Direction (SPWD~~). First numerical results about glazed-surface albedo are thus provided, which is found to be lower than the surrounding snow, especially in NIR wavelengths. This detailed information~~), useful for mapping them. These parameters allowed us to characterise and perform ~~a precise mapping~~ an automated detection of the glazed surfaces, and we determined the influence of the SPWD by including it and excluding it from the detection approach. The exclusion of the SPWD resulted in an 88% overestimation in the detection of glazed surfaces. Using remote and field observations, for the first time we surveyed all the components of upwind migration (absolute, sedimentological and ice flow), with an absolute value of about 10 m a^{-1}. The analysis shows that the migration is driven by the snow accumulation on the crest and ~~their evolution and trends over time, demonstrating a general overall intra-annual areal decrease in summer (-16%) and an inter-annual increase over recent years (at maximum almost +0.2% per year in January).~~ through prograding upwind on the previous windward flanks characterised

by glazed surface. Our results present significant implications for Surface Mass Balance estimation, paleoclimate reconstruction using ice cores and for the measurements using optical and radar images/data in the megadune area.

1 Introduction

Antarctic climate and mass balance have been highlighted by the Special Report on the Ocean and Cryosphere in a Changing Climate (Meredith et al., 2019) by the Intergovernmental Panel on Climate Change (IPCC) among the main uncertainties for the climate system and sea level projections. Surface mass balance (SMB) is the net balance between the processes of snow accumulation and loss on a glacier surface and provides mass input to the surface of the Antarctic Ice Sheet. Therefore, it represents an important control on ice sheet mass balance and resulting contribution to global sea level change. Ice sheet SMB varies greatly across multiple scales of time (hourly to decadal) and space (meters to hundreds of kilometres), and it is notoriously challenging to observe and represent in atmospheric models. Moreover, given the difficulties in accessing the interior of the ice sheet, only limited field observation on past and current conditions exists. The part of the East Antarctic Ice Divide closest to the South Pole is the coldest and driest area on Earth and presents several unique features (e.g. megadunes, glazed surfaces etc.) and processes (e.g. extensive post-depositional effects in the snow as well as interactions between the snow surface and the overlying atmosphere) that remain relatively unexplained (Fahnestock et al., 2000; Frezzotti et al., 2002a, b; Courville et al., 2007; Scambos et al., 2012). The glazed surface or wind crust areas show a local net SMB close to zero, in contrast with the rest of the continent where SMB is mainly positive (Agosta et al., 2019), which leads to characteristics of the surface that can be observed from the satellites (Fahnestock et al., 2000; Scambos et al., 2012). Megadune morphologies form through the interaction of peculiar conditions of snow accumulation and metamorphism, wind, and topography. Previous works have already studied megadune fields in Antarctica using ground penetration radar (GPR; Frezzotti et al., 2002a, b; Arcone et al., 2012a, b; Das et al., 2013; Ekaykin et al., 2015), atmospheric models (Dadic et al., 2013; Palm et al., 2011, 2017) and remote sensing, both at high resolution (Frezzotti et al., 2002a, b; Traversa et al., 2021a), based on previous satellites of the Landsat family, and lower spatial resolution by using other images (Das et al., 2013), such as Radarsat/MODIS (Fahnestock et al., 2000; Arcone et al., 2012a; Scambos et al., 2012) and AVHRR (Fahnestock et al., 2000). However, a detailed analysis of megadune physical parameters and their migration over time is still lacking.

This study focuses mainly on satellite image analysis of two megadune areas of the East Antarctic Ice Sheet (EAIS) situated respectively 300 km East of Vostok Station and 150 km East of Concordia Station (both areas are located in the same huge megadune field, approximately 450,000 km^2, Fahnestock et al., 2000, Fig.1), characterized by the presence of megadune formations. Both areas were crossed and surveyed by two snow traverses respectively in the 2018-19 EAIIST expedition (East Antarctic International Ice Sheet Traverse) and 1998-1999 It-ITASE (Italian-International TransAntarctic Scientific Expedition) expedition. The analysis of survey data of the first area (EAIIST, 300 km East of Vostok Station, https://www.eaiist.com/en/) are under process whereas the in situ observations of the second traverse It-ITASE are available (Frezzotti et al., 2002a, b, 2004, 2005; Proposito et al., 2002; Vittuari et al., 2004).

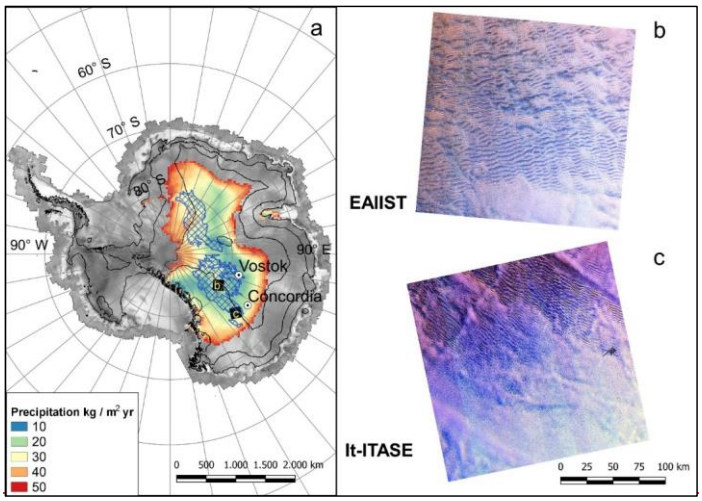

~~**Figure 1: Antarctic continent with the zoom (see b and c in panel a) of the study areas, i.e., EAIIST (b) and It-ITASE (c, with the traverse transects in black) tile of Landsat (false colour composites). In the background (a): surface elevation contour lines every 1000 m, RAMP Radarsat Mosaic (Jezek, 1999), RACMO total precipitation rate (Van Wessem et al., 2014) and megadune fields as blue reticulate polygons (Fahnestock et al., 2000). Polar Stereographic projection.**~~

~~The aim of the study is to provide a detailed survey on megadunes of the Antarctic continent by remote sensing, considering different physical parameters captured through Landsat 8 OLI satellite images at 15/30 m spatial resolution. Our study focuses on two Landsat tiles, i.e. 069119 (EAIIST site, Lat 80°47' S Long 122°19' E) and 081114 (It-ITASE site, Lat 75°54' S Long 131°36' E), in order to provide new information about different parameters of megadune fields: dune migration, albedo (spectral and broadband), brightness temperature and morphologies. A mapping of glazed surfaces associated to these megadune fields is provided, based on the above-mentioned parameters.~~

~~1.1 Megadune fields~~

~~Megadunes were first described by Swithinbank (1988), who termed these features based on their likeness to transverse sand megadunes on satellite images. They rise a few meters above the general surface level and are imperceptible to the surface traveller. When viewed from an airplane or satellite, these features appear as long waves of alternating blueish (glazed surface) and white bands (sastrugi). The surface waveforms with regular bands of sastrugi and glazed surfaces allow surveying the megadunes by satellite observations, because of differences in albedo (Frezzotti et al., 2002a) and microwave backscatter (Fahnestock et al., 2000). These features are widespread in the remotest areas of the southern part of the East Antarctic Ice~~

Divide and extend for more than 500,000 km² (Fahnestock et al., 2000; Frezzotti et al., 2002a), as a result of uncommon snow accumulation and redistribution processes; thus, they have a crucial role in SMB and ice core interpretation. In fact, in such inland areas, the stability of climatic conditions could play a key role in megadune formation, since accumulation is very low while katabatic wind intensity and direction are stable; these conditions could affect snow sintering and a high grade of snow metamorphism (Albert et al., 2004; Courville et al., 2007; Scambos et al., 2012; Dadic et al., 2013). The climatic conditions of megadune fields are characterized by extremely low temperatures (mean annual temperatures from −45° to −60°C), extremely low snow accumulation (<50 mm water equivalent per year, w.e.a^{-1}). Megadunes are oriented perpendicular to the slope along the prevailing wind direction (SPWD), wave amplitudes are small (about 1-4 m), wavelengths range from 2 to over 5 km with a 3 km average (amplitude and wavelength statistics are here calculated using almost fifty megadunes sampled in the transects at the EAIIST site, Fig. 2), and megadune crests are nearly parallel, extending from tens to hundreds of kilometres (Swithinbank, 1988; Fahnestock et al., 2000; Frezzotti et al., 2002a, b; Arcone et al., 2012a, b). The angle between the wind direction (50° - 60°) and the direction of general surface slope (95° - 100°) at a regional scale is about 40° - 50° at It-ITASE (Frezzotti et al., 2002b) and about 30° - 50° at EAIIST with 40° - 50° of wind direction and 80° - 85° of aspect. This clearly shows the katabatic flow draining from the high plateau and turning to the left under the action of the Coriolis force. For these reasons, the directions of megadunes and sastrugi are fundamental in order to evaluate the local orientation of prevalent wind direction (Mather, 1962; Parish and Bromwich, 1991; Fahnestock et al., 2000). At kilometre scale, regional SPWD in the megadune area was calculated by Frezzotti et al. (2002b) as 0.10 – 0.15% (1.0 – 1.5 m km^{-1}), less than half of the megadune leeward face slope of 0.4–0.5% (4–5 m km^{-1}).

Based on previous studies, the SMB range is 25% (leeward faces, characterized by the presence of wind glazed surfaces, as described later) and 120% (windward faces, covered by huge sastrugi up to 1.5 m height) of accumulation in adjacent non-megadune areas (Frezzotti et al., 2002b). In addition, the sedimentary structure of buried megadunes examined via ground penetrating radar (GPR) suggests that the sedimentary morphology of the windward face (sastrugi) migrates upwind with time, burying the glazed surface of the leeward face (Frezzotti et al., 2002b; Ekaykin et al., 2015), in contrast with sand dunes (which show a downward migration) and typical of "antidune" formations of fluvial and ocean bedforms (Prothero and Schwab, 2004). This uphill migration is caused by the difference in accumulation between windward (high accumulation) and leeward (near-zero accumulation) sides, also leading to differences in snow features and surface roughness (Fahnestock et al., 2000; Albert et al., 2004; Courville et al., 2007). According to Dadic et al. (2013), who based his analysis on superficial flow theory for sediments in water (Núñez-González and Martín-Vide, 2011) and atmospheric flow modelling, persistent katabatic winds, strong atmospheric stability and spatial variability in surface roughness are the primary controllers of upwind accumulation and migration of megadunes, where the latter represents the main factor that influences their velocity. In association with megadunes, wide glazed surfaces are present in the region where the SPWD is higher than 0.25° (0.4% or 4 m km^{-1}). Glazed surface area shows deep cracks that are more evident in the early summer season (Watanabe, 1978; Frezzotti et al., 2002a; Albert et al., 2004; Courville et al., 2007), caused by repeated thermal cycles (thermal expansion and contraction of snow or firn layers), and patterns with polygonal forms, correlated to a long-term hiatus in accumulation of snow (Watanabe, 1978).

4

Fortunately, the spectral differences between glazed areas and surrounding snow make their identification easier from space, as the former have a lower albedo (Fujii et al., 1987; Frezzotti et al., 2002a; Scambos et al., 2012). Spectral differences also lead to an effect on temperatures, which is on average higher than on the snow surface (Fujii et al., 1987). Megadunes appear to be formed by an oscillation in the katabatic air flow, leading to a wave-like variation in net accumulation. The wind-waves are formed at the change of SPWD, in response to the buoyancy force, favouring the standing-wave mechanism (Fahnestock et al., 2000; Frezzotti et al., 2002b).

2 Materials and Method

2.1 Materials

In order to study the megadunes and glazed areas, we used Landsat 8 OLI satellite images from 2013 to 2021 (https://earthexplorer.usgs.gov/). Landsat 8 provides data in several spectral bands, including visible (0.45-0.67μm, bands 2-3-4) near infrared (NIR, 0.85-0.88 μm band 5) and short-wave infrared (1.57-2.29 μm bands 6-7), at 30 m spatial resolution, with three more bands at different spatial resolution: a panchromatic band (0.503-0.676 μm, 15 m, band 8) and two thermal infrared bands (10.6-12.51 μm, 100 m, bands 10-11). In this study, we used all the VIS and IR bands (from 2 to 7) to calculate albedo and map megadunes, thermal bands to calculate brightness temperature and the panchromatic band to perform the megadune migration analysis. Excluding from our dataset all images with cloud cover > 10% of land surface and visible blowing snow events, we obtained 21 images from Landsat 8 during the period of satellite observation (Table A1), 14 for the EAIIST site and 7 for It-ITASE. Cloud cover was detected using the value reported in the Landsat Metadata, which is determined by the CFMask (C code of the Function of Mask) algorithm (Foga et al., 2017) and, since it may be inaccurate over bright targets as snow, an additional visual check for each analysed image was performed. For the calculation of megadune migration (Sect. 2.2.4), also Sentinel-2 optical imagery (Band 8 NIR) was used. Sentinel-2 images were acquired using the same criteria as for Landsat, with the advantage of having a higher spatial resolution of 10 m.

In addition, we extracted wind direction from ERA5 (Hersbach et al., 2020) and by identification of sastrugi based on Landsat (Sect. 2.2.3). ERA5 is distributed by the European Centre for Medium-Range Weather Forecasts (ECMWF) and is an atmospheric reanalysis global climate dataset. In particular, we used *hourly data* (DOI: 10.24381/cds.adbb2d47). The wind speed and direction were obtained by combining 10-m u and v wind components, and averaged on a 20-year temporal period, from 2000 to 2019. In ERA5 u and v are calculated as:

$$u = -|\vec{V}| \sin\phi$$
$$v = -|\vec{V}| \cos\phi \quad (1)$$
$$\vec{V} = \sqrt{u^2 + v^2}$$

and ϕ is the meteorological wind direction (direction from where the wind is blowing, with 0° = N and increasing clockwise).

Antarctic climate and mass balance have been highlighted by the Special Report on the Ocean and Cryosphere in a Changing Climate (Meredith et al., 2019) by the Intergovernmental Panel on Climate Change (IPCC) among the main uncertainties for the climate system and sea level projections. Surface mass balance (SMB) is the net balance between the processes of snow precipitation and loss on a glacier surface and provides mass input to the surface of the Antarctic Ice Sheet. Therefore, it represents an important control on ice sheet mass balance and resulting contribution to global sea level change. Ice sheet SMB varies greatly across multiple scales of time (hourly to decadal) and space (metres to hundreds of kilometres), and it is notoriously challenging to observe and represent in atmospheric models (Agosta et al., 2019). Moreover, given the difficulties in accessing the interior of the ice sheet, only limited field observation on past and current conditions exists. The Southern part of the East Antarctic Ice Divide, from Concordia and Vostok Stations to the South Pole is the coldest and driest area on Earth and presents unique features called megadunes, which extend for more than 500,000 km^2 (Fahnestock et al., 2000). The drivers of megadune formation are uncommon snow accumulation and redistribution processes driven by wind scouring that remain relatively unexplained (Fahnestock et al., 2000; Frezzotti et al., 2002a, b; Courville et al., 2007; Scambos et al., 2012; Dadic et al., 2013; Ekaykin et al., 2015, Fig. 1). Ground surveys of megadunes show that snow is removed from their leeward slopes where a specific erosional type of snow, "glazed surface" or "wind crust", is formed as a result. In contrast, snow accumulation is increased on the windward slopes that are characterised by the depositional types of the snow microrelief termed "sastrugi". Glazed surfaces form because wind and sublimation can ablate much more snow/firn than is accumulated by annual solid precipitation, causing a persistent SMB close to zero or negative. The stability of climatic conditions could play a key role in megadune formation, since accumulation is very low while katabatic wind intensity and direction are stable; these conditions affect snow sintering and a high grade of snow metamorphism (Albert et al., 2004; Courville et al., 2007; Scambos et al., 2012; Dadic et al., 2013). Megadunes are oriented perpendicular to the Slope along the Prevailing Wind Direction (SPWD), wave amplitudes are small (up to 8 m), wavelengths range from 2 to over 5 km and megadune crests are nearly parallel, extending from tens to hundreds of kilometres (Swithinbank, 1988; Fahnestock et al., 2000; Frezzotti et al., 2002a, b; Arcone et al., 2012a, b). The angle between the katabatic wind direction and the direction of general surface slope at a regional scale can differ up to 50° due to the interaction between the topographic slope driving gravity and the Coriolis force (Fahnestock et al., 2000; Frezzotti et al., 2002b).

Based on previous studies, the SMB of megadunes ranges between 25% (leeward faces glazed surfaces) and 120% (windward faces, covered by huge sastrugi up to 1.5 m in height) of accumulation in adjacent non-megadune areas (Frezzotti et al., 2002b). The sedimentary structure of buried megadunes examined via Ground Penetrating Radar (GPR) and Global Position System (GPS) suggests that the sedimentary morphology of the windward face (sastrugi) migrates upwind with time, burying the glazed surface of the leeward face (Frezzotti et al., 2002b; Ekaykin et al., 2015), with typical "antidune" processes similar to those observed on fluvial and ocean bedforms (Prothero and Schwab, 2004). This uphill migration is caused by the difference in accumulation between windward (high accumulation) and leeward (near-zero or negative accumulation) sides, also leading to differences in snow features and surface roughness (Fahnestock et al., 2000; Frezzotti et al., 2002a; Albert et al., 2004; Courville et al., 2007). Megadunes appear to be formed by an oscillation in the katabatic air flow, leading to a wave-like

variation in net accumulation; the wind-waves are formed at the change of SPWD, in response to the buoyancy force, favouring the standing-wave mechanism (Fahnestock et al., 2000; Frezzotti et al., 2002b). According to Dadic et al. (2013), who based his analysis on superficial-flow theory for sediments in water (Núñez-González and Martín-Vide, 2011) and atmospheric flow modelling, persistent katabatic winds, strong atmospheric stability and spatial variability in surface roughness are the primary controllers of upwind accumulation and migration of megadunes, where the latter represents the main factor that influences their velocity.

The surface waveforms of megadunes with regular bands of sastrugi and glazed surfaces allow surveying the megadunes by satellite observations, because of differences in albedo and microwave backscatter (Fahnestock et al., 2000; Frezzotti et al., 2002a; Scambos et al., 2012) between these features and surrounding snow. Spectral differences also lead to an effect on temperatures, which is on average higher than on the snow surface (Fujii et al., 1987). In spite of the importance of the glazed surfaces of megadunes for the SMB of Antarctica, a remote sensing characterization of their physical properties and spatial distribution, and a quantitative analysis of their migration is currently lacking. The aim of the study is to provide a detailed survey of the spatial and temporal variability of two megadune areas using remote sensing data (Landsat 8 and Sentinel-2), elevation models (Reference Elevation Model of Antarctica REMA, Howat et al., 2019) and climatic conditions using atmospheric reanalysis data (ERA5) in addition to past in-situ measurement data (firn core, GPR and GPS), to explore spectral, thermal, and windward slope relationships with a view towards generating an algorithm for their automatic detection. Moreover, we provide for the first time the first calculation of the absolute megadune movement, and its different components: ice-flow and sedimentological progradation. The analysis of absolute megadune movement has important implications on the remote sensing ice dynamic measurements, in particular on ice flow measurements and elevation changes.

1.1 Study area

Megadune fields on the Antarctic continent extend along 10° in latitude (75°-85°S, about 1100 km) and 30° in longitudine (110°-140° E, about 300-600 km). The climatic conditions of the area are characterised by extremely low temperatures (mean annual temperatures from –45° to –60°C), extremely low snow precipitation (<30 mm water equivalent per year, $w.e.a^{-1}$; Van Wessem et al., 2014; Agosta et al., 2019) and nearly constant katabatic wind direction and wind speed (6–12 m s^{-1}; Courville et al., 2007). Analysis of data acquired by the Cloud-Aerosol Lidar and Infrared Pathfinder Satellite Observation (CALIPSO) satellite has enabled the construction of a 12-year climatology of blowing snow over Antarctica, showing that the greatest frequency of blowing snow events, approaching 75% of observations, is seen in the megadune region (Palm et al., 2019).

This research focuses on two megadune areas that were crossed and surveyed by two snow traverse expeditions: EAIIST (East Antarctic International Ice Sheet Traverse) in 2018-19 and It-ITASE (Italian-International TransAntarctic Scientific Expedition) in 1998-1999. EAIIST area is situated 300 km East of Vostok Station (centred at 80°47'S 122°19'E) and It-ITASE area 150 km East of Concordia Station (centred at 75°54'S 131°36'E; Fig. 1). The survey data of the first area (EAIIST, https://www.eaiist.com/en/) are under processing whereas the in situ observations of the second traverse It-ITASE are available (Frezzotti et al., 2002a, b, 2004, 2005; Proposito et al., 2002; Vittuari et al., 2004). The EAIIST area is in the middle of the

megadune area; thus, megadunes are well defined and continuous on satellite images in optical and microwave bands, whereas the It-ITASE area is at the North-East limit of the megadune field where this morphology is discontinuous and disappears, thus representing the developing threshold of the environmental conditions (morphology, climatology, glaciology) determining megadune formation.

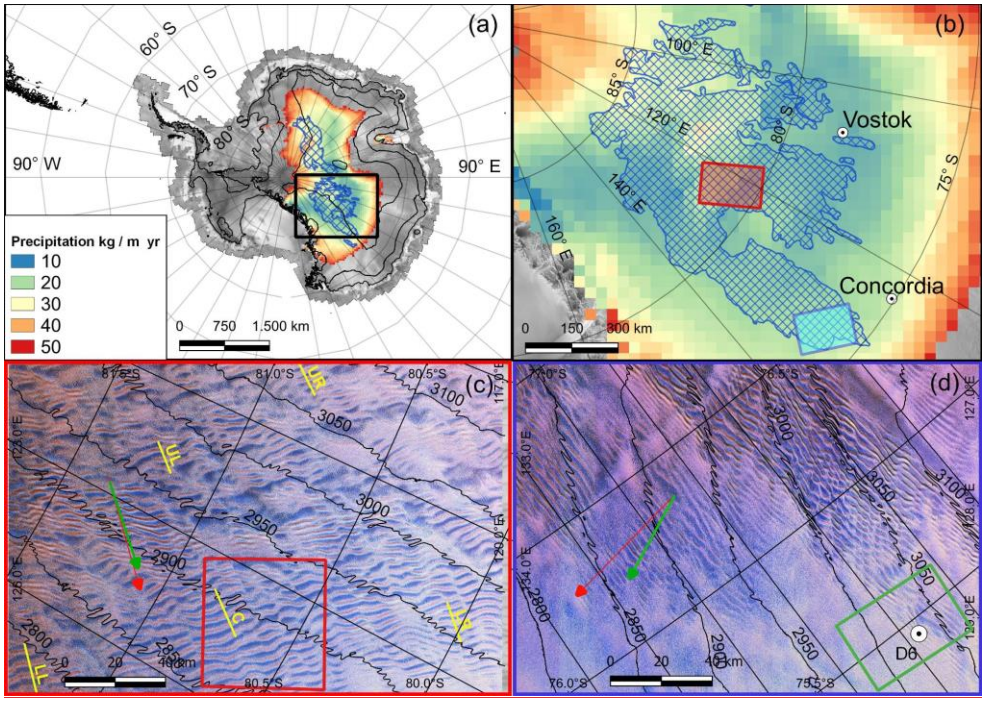

Figure 1: Location map of megadune area: (a) Satellite image map of the Antarctic continent (Jezek, 1999) with elevation contour lines at 1000 m a.s.l. intervals, megadune regions are shown as cross-hatched blue areas (Fahnestock et al., 2000), with snow precipitation by RAMCO in colour for areas with precipitation < 50 kg m^2 a^{-1} (Van Wessem et al., 2014), black rectangle (b box). (b) The megadune field with two study sites, EAIIST red rectangle (c box) and It-ITASE blue rectangle (d box). (c) Landsat 8 OLI image in false colour (069119 scene, 17/Dec/2015) of the EAIIST area; the red polygon is the area for the analysis of variations of glazed surfaces (Fig. 4). (d) Landsat 8 OLI image in false colour (081114 on 18/Dec/2014) of the It-ITASE area and D6 core site; the green rectangle shows the location of Fig. 5. In (c) and (d) boxes, red arrows represent ERA5 wind direction and green arrows sastrugi-based wind direction, while the yellow lines show the location of the transects studied.

Topographically, the two study areas are in a relative sloping zone where the altitude decreases moving from SW to NE and the elevation ranges from 2700 to 3200 m a.s.l. Thus, the topographic aspect (the direction that a topographic slope faces) is generally East (~ 80°, It-ITASE and ~ 70°, EAIIST). The regional topographic slope (10 km scale) is on average 1.5 m km^{-1} and 1.8 m km^{-1} for the It-ITASE and EAIIST areas, respectively. The katabatic wind direction is nearly constant with wind blowing from SW in both areas.

2 Data and Methods

2.1 Data

In order to study the megadune areas, we combined three main datasets (satellite images, meteorological data from reanalysis products, DEM) to create a method for the automatic detection of snow glazed surfaces. We further created 5 sample transects in the EAIIST area (Fig. 1c) and visually identified thresholds of albedo, thermal brightness temperature and SPWD to discriminate between glazed surfaces and surrounding snow. The 5 transects were created in different areas of the megadune field and they show relatively different wind directions and topographic aspect and slope, with the aim of representing the widest possible range of SPWD values.

2.1.1 Satellite datasets

Two sources of satellite imagery were used: Landsat 8 OLI satellite images and Sentinel-2 images, both downloaded from the Earth Explorer portal (https://earthexplorer.usgs.gov/). Landsat 8 OLI and Sentinel-2 provide data in several spectral bands, including panchromatic, visible, very near infrared, short-wave infrared, and thermal infrared bands, with different spatial resolution from 10 to 100 m. Satellite images from Landsat 8 OLI (supplementary Table A1) were chosen at dates close to the first stripe acquisitions of the REMA DEM (2013, Table A2). The megadune area is subject to blowing snow events (more than 75% of the time; Palm et al, 2019) and cloud cover. Moreover, in the morning a strong atmospheric inversion layer develops 70 % of the time during summer on the Antarctic plateau (Pietroni et al., 2014) with the formation of fog, which is not homogeneously distributed on the area surveyed by satellite images and is difficult to detect. Therefore, we excluded from our dataset all images with cloud cover > 10% of land surface, visible blowing snow and fog events and images with solar zenith angle (SZA) ≥ 75° (because of the effect on the albedo, as demonstrated by Picard et al., 2016), and obtained 17 images from Landsat 8 from 2013 to 2020 and 4 images from Sentinel-2 from 2018 to 2021 (Table A1), 11 for the EAIIST site and 6 for It-ITASE. To map glazed surfaces on megadunes, we used Landsat 8 OLI data as the method relies on the calculation of the albedo, which has been thoroughly validated for Landsat 8 OLI (Traversa et al., 2021a). Additionally, Landsat 8 OLI is available for a longer period of time compared to Sentinel-2, allowing us to investigate temporal evolution of the megadune area. In the megadune area, the difference between snow glazed surfaces and snow is higher considering NIR spectral albedo and brightness temperature (Traversa et al., 2021b). To a "higher" amount of solar radiation absorbed by the glazed surface, corresponds also a different brightness temperature on snow glazed surfaces (Fujii et al., 1987; Scambos et al., 2012 and

references therein). In fact, these zones show a higher brightness temperature compared to the upwind part of the dune characterised by the snow surface. In detail, we used Landsat 8 OLI Near InfraRed band (NIR band 5, with a ground resolution of 30 m) to calculate NIR albedo and thermal infrared (TIRS 1) band 10 to calculate brightness temperature (with a ground resolution of 100 m, provided resampled to 30 m). To perform the megadune migration analysis (sect 2.2.2), we used the panchromatic band of Landsat 8 OLI, as this band has a higher resolution (15 m) compared to the other spectral bands of the Landsat. For comparison, Sentinel-2 images were also used, specifically Band 8 NIR (10 m spatial resolution), which allows better observing differences between snow and glazed surfaces compared to the other visible and infrared bands.

2.1.2 Atmospheric reanalysis dataset

We extracted wind direction from the ERA5 atmospheric reanalysis global climate dataset (Hersbach et al., 2020) and by identification of sastrugi based on Landsat (Sect. 2.2.1). In particular, we used ERA5 *hourly data* (DOI: 10.24381/cds.adbb2d47) of wind speed and direction at 10 m above the surface averaged over a 20-year temporal period, from 2000 to 2019. Beside using all wind speed observations, we further divided wind speed in 5 classes, only considering wind speed values above specific thresholds~~:~~, i.e., wind speed >3 m s^{-1}, >5 m s^{-1}, >7 m s^{-1} and >11 m s^{-1}. These thresholds were chosen based on the interactions between wind and snow: snow transportation by saltation (within 0.3 m in elevation) starts at wind speeds between 2 and 5 m s^{-1}, transportation by suspension (drift snow) starts at velocities > 5 m s^{-1} (within 2 m) and blowing snow (snow transportation higher than 2 m) starts at velocities between 7 and 11 m s^{-1} (see ~~Frezzotti et al., 2004 and references therein).~~Frezzotti et al., 2004 and references therein). The threshold wind speed at which the sublimation of blowing snow starts to contribute substantially to katabatic flows in a feedback mechanism appears to be 11 m s^{-1} ~~(Kodama et al., 1985; Wendler et al., 1993).~~(Kodama et al., 1985; Wendler et al., 1993).

~~Finally, in order to obtain aspect and slope of the surface for the SPWD calculation and perform topographic correction for the calculation of albedo, we used the Reference Elevation Model of Antarctica (REMA, Howat et al., 2019) digital elevation model (DEM; www.pgc.umn.edu/data/rema/). This DEM provides the first high spatial resolution (8 m) terrain map using hundreds of thousands of individual stereoscopic pairs of submeter (0.32 and 0.5 m) DigitalGlobe satellite imagery. Each individual DEM was vertically registered to satellite altimetry measurements from Cryosat-2 and ICESat, resulting in absolute uncertainties of less than 1 m. It is based mainly on 2015-2016 imagery acquired during the austral summer period (December-March) (Howat et al., 2019). At the EAIIST site, the temporal period is slightly wider (from 2008 to 2017), although 86% of stripes were acquired in 2013-2017 (Table A2).~~

2.1.3 Topographic dataset (DEM)

In order to obtain the aspect and slope of the surface for the SPWD calculation and perform topographic correction for the calculation of albedo, we used a mosaic of REMA tiles (www.pgc.umn.edu/data/rema/; Howat et al., 2019). These are constructed from thousands of individual stereoscopic Digital Terrain Models (DEMs) at high spatial resolution (8 m). Each individual DEM was vertically registered to satellite altimetry measurements from Cryosat-2 and ICESat, resulting in absolute

uncertainties of less than 1 m, and relative uncertainties of decimeters. REMA is based mainly on imagery acquired during the austral summer period (December-March) and at the two sites, the temporal period is from 2008 to 2017, although 87.5% of stripes were acquired in 2013-2017 (Table A2).

2.2 Methods

~~Considering our aims, the study includes four main processing steps: Landsat 8 OLI image processing for the calculation of spectral and broadband albedo; extraction of brightness temperatures from Landsat thermal bands; SPWD calculation from ERA5 (Hersbach et al., 2020) and sastrugi-based wind direction; estimation of the superficial speed of megadunes and the direction and intensity of their migration over time.~~

~~To characterize wind glazed areas and megadunes~~The study includes four main processing steps: Landsat 8 OLI image processing for the calculation of NIR albedo; extraction of thermal brightness temperatures from the Landsat thermal band 10; SPWD calculation from ERA5 and satellite sastrugi-based wind direction, estimation of the surface velocity and migration of megadunes using feature tracking (2014-2021) and comparison of GPR-GPS measurements from 1999 with the REMA DEM from 2014 (specific strip on the area). The first three steps were at the basis of the automatic detection of the snow glazed areas.

2.2.1 Automatic detection of glazed snow surfaces

Taking advantage of the spectral and topographic datasets employed, we ~~chose dates that corresponded with the first stripe acquisitions of the REMA DEM (2013, Table A2). We further created 7 sample transects (5 in the EAIIST area and 2 at It ITASE) (Fig.2) and 30 polygons (equally subdivided in the EAIIST and It ITASE~~ **consider for the automatic detection of the glazed areas**~~) and performed statistical calculations to identify thresholds of~~ **the following parameters: NIR albedo, thermal brightness temperature and SPWD** ~~to discriminate between glazed surfaces and surrounding snow. The seven transects are in different areas of the megadune field and they show different wind directions, with the aim of representing the widest possible range of SPWD values.~~. **The** ~~transect plots in the paper refer to weighted moving averages based on 11 transect pixels. Each plot is associated to a normalized plot that presents also detrended topography to remove the effect of the topographic slope. Finally, we used Pearson's correlation coefficient to determine the strength of the relationship between the above-mentioned parameters.~~

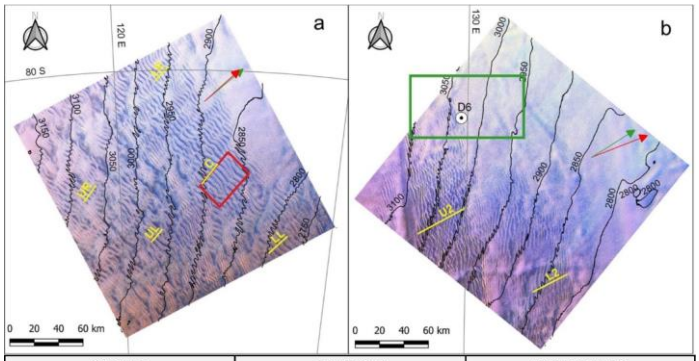

Transect	Length (km)	Angle from North
C	20	39°
LL	20	47°
LR	16	43°
UL	13	39°
UR	16	35°
U2	42	60°
L2	30	63°

~~**Figure 2: Locations of transects (yellow) on the false colour images of the EAIIST site (a, Lat 80°47' S Long 122°19' E) and It-ITASE site (b, 75°54' S Long 131°36' E). Red rectangle (a) is the area for the analysis of variations of glazed surfaces (Fig.7) and green rectangle (b) is the zoom in of Fig.3a; green arrows ERA5 wind direction and red arrows sastrugi-based wind direction. Transect length and angle from North (lower panel). Universal Transverse Mercator (UTM) projections.**~~

~~2.2.1 Spectral and broadband Albedo calculation~~

~~The~~NIR albedo (α), ~~also called bi-hemispherical reflectance, is defined as the ratio of the radiant flux reflected from a unit surface area into the whole hemisphere to the incident radiant flux of hemispherical angular extent (Schaepman-Strub et al., 2006) in the approximate spectral range 350–3000 nm (Bishop et al., 2011). In this study the albedo, both spectral and broadband, was~~was here estimated using Landsat 8 OLI imagery, following the method ~~firstly~~first proposed by ~~Klok et al. (2003), then adjusted by Fugazza et al. (2016)~~Klok et al. (2003) and recently tested and validated in Antarctica by ~~Traversa et al. (2021b). In order to obtain the albedo of the sample area, Landsat images need to be processed and corrected. In fact, originally Landsat provides quantized digital numbers (DN, dimensionless) that need to be scaled back to radiance and then converted to Top of Atmosphere (TOA) reflectance. Here, TOA reflectance conversion was performed by using the solar zenith band (obtained from the Angle file of Landsat 8, see Landsat 8 Data User Handbook, Zanter, 2019). This conversion allows applying a more accurate per-pixel correction for the solar zenith angle (SZA), useful in our study considering the average high SZA (>60°), typical of inner Antarctica, and its strong effect on albedo (Pirazzini, 2004; Picard et al., 2016; Traversa et al., 2019). TOA reflectance was then corrected for atmospheric and topographic effects (Klok et al., 2003; Fugazza~~

et al., 2016; Traversa et al., 2021b). For the atmospheric correction, we used the 6S radiative transfer code (Vermote et al., 1997), using the *i.atcorr* tool of GRASS GIS with an aerosol optical thickness (AOT) at 550 µm of 0.02, based on the values from the AERONET Aerosol Robotic Network (https://aeronet.gsfc.nasa.gov/cgi-bin/draw_map_display_aod_v3) at Concordia Station (the closest station to our study areas). As regards topographic correction, we used the *i.topo.corr* tool of GRASS GIS with the c-factor method. During these last two steps, the REMA DEM was resampled to 30 m using bilinear interpolation. For a more detailed description of these correction steps, refer back to Traversa et al. (2021b). Finally, narrowband to broadband albedo conversion was carried out by using Liang algorithm (Liang, 2001), applied on bands 2-4-5-6-7 of Landsat 8. The algorithm is:Traversa et al. (2021a). We used NIR albedo as opposed to broadband albedo owing to the higher detection ability of NIR albedo, which stems from the fact that broadband albedo obtained by using Liang conversion algorithm (Liang, 2001) considers the visible area of the spectrum and the shortwave infrared. In fact, in broadband albedo it is hardly possible to recognize the differences between glazed and unglazed areas, which in the visible wavelengths look very similar (Warren, 1982).

$$\alpha = 0.356\alpha_2 + 0.130\alpha_4 + 0.373\alpha_5 + 0.085\alpha_6 + 0.072\alpha_7 - 0.0018 \quad (2)$$

where α_x is the spectral albedo of each band and xFollowing the methodology proposed by Traversa et al. (2021a, c), the images were processed through three main steps: 1) conversion of radiance to Top of Atmosphere (TOA) reflectance by using per-pixel values of the SZA available through the Landsat solar zenith band. This conversion allows applying a more accurate per-pixel correction for the SZA, useful in our study considering the average high SZA (always ≥ 59°, Table A1), and its strong effect on albedo (Pirazzini, 2004; Picard et al., 2016; Traversa et al., 2019); 2) atmospheric correction; 3) topographic correction.

To retrieve the thermal brightness temperature, we employed the band number.

2.2.2 Brightness temperature calculation

As regards the retrieval of temperature, we employed the thermal bands of Landsat 8 OLI, i.e. bands 10 and 11.10 of Landsat 8. To estimate the TOA thermal brightness temperature received at the satellite, spectral radiance in the thermal bandsband was converted using the thermal constants in the Landsat metadata. The TOA brightness temperature is calculated as follows: (Zanter, 2019).

$$T = \frac{K_2}{ln\left(\frac{K_1}{L_\lambda}+1\right)} \quad (3)$$

where T isFor the TOA brightness temperature in Kelvin, L_λSPWD, the TOA spectral radiance and $K_{1,2}$ the band specific thermal conversion constants from the Landsat Metadata.

~~2.2.3 Calculation of Slope along the prevailing wind direction (SPWD)~~

~~The SPWD is one of the most important parameters that characterizes megadune fields (Frezzotti et al., 2002b) and depends on wind direction and surface slope. As regards the first parameter, i.e. wind direction, we~~ wind directions were extracted ~~it from ERA5. Since ERA5 has a~~ at low spatial resolution (30 km~~), we also calculated sastrugi directions to derive wind orientation, as they are parallel to it (Mather, 1962; Parish and Bromwich, 1991; Fahnestock et al., 2000; Frezzott et al., 2002a and b). Sastrugi based~~) using ERA5 and validated by identifying sastrugi and deriving wind directions ~~were used to validate ERA5 values and were extracted from~~from them using Landsat 8 OLI at 30 m spatial resolution~~. In a first step, we generated False Colour Composites (FCC) of~~ (Mather, 1962; Parish and Bromwich, 1991). The identification of sastrugi was performed on the Landsat 8 OLI ~~bands 3, 4 and 5 (Green, Red and~~ NIR ~~respectively) which allowed observing differences between snow, glazed surfaces, dunes and sastrugi.~~

~~Subsequently, in order to highlight the differences among these morphologies and better identify the sastrugi, we applied a Principal Component Analysis (PCA) on the FCC (~~*i.pca* module in GRASS GIS, Richards and Richards, 1999). ~~Then, on the first principal component raster, where Band 5 NIR already explained over 90% of the variance on average (solar radiation is strongly absorbed in this part of the spectrum on glazed surfaces and, in contrast with the visible bands, here feature differences are highlighted, Frezzotti et al., 2002b), we applied an~~band (band 5) by applying the Canny edge detection algorithm (*i.edge* in GRASS GIS, ~~Canny, 1986), with the aim of excluding other features and highlight sastrugi only.~~Canny, 1986). Prior to edge detection, each image was pre-processed by using a high pass filter with a length scale of 150 m implemented through a Fast Fourier Transform to highlight the sastrugi. This process was applied on 7 Landsat scenes from the spring~~,~~ and summer ~~and fall~~ months i.e., ~~October,~~ November, December and January of the period ~~2014~~2013-2020~~). Only small differences were found in these scenes, confirming the stability in direction of sastrugi landforms and thus of katabatic winds. Finally, to obtain a complete map of wind direction, comparable to the one of ERA5, we applied surface interpolation.~~.

To further ~~calculate~~estimate the SPWD based on the wind direction from ERA5 and Landsat-derived sastrugi, we ~~implemented a specific algorithm. For each pixel,~~used the ~~SPWD was~~approach of Scambos et al. (2012), i.e., we calculated ~~by taking one of~~ the ~~adjacent pixels to calculate~~dot product between the ~~altitude difference, following~~slope derived from the REMA DEM and the wind direction~~, following Eq. (4).~~. The algorithm was applied to ERA5 and sastrugi-based wind directions resampled at 120 m spatial resolution, and the REMA DEM was resampled to match ERA5 and sastrugi-based wind directions using bilinear interpolation. The resulting SPWD has units of m km^{-1}.

~~$$SPWD(i,j) = 1000\frac{(h(i+k,j+l)-h(i,j))}{d} \quad (4)$$~~

~~where $h(i,j)$ is the elevation of a given pixel, and k and l are coefficients $\in \{-1,0,1\}$ used to select the adjacent pixel along the wind direction. k = -1 for NW, N and N, zero for E and W and +1 for SW, S and SE. l = -1 for NW, W and SW, 0 for N and S and +1 for NE, E and SE. d is calculated as the x-y distance between two pixels. The resulting SPWD has units of m km^{-1}.~~

~~The choice of using 2 pixels was taken to avoid an excessive flattening of the SPWD, that would be obtained using a more conventional slope algorithm (using 9 pixels).~~

Due to the small difference in NIR albedo and brightness temperature and the different illumination and meteorological conditions inside the satellite images, the analysis of the variability of SPWD, NIR albedo and brightness temperature was conducted in detail on the 5 transects perpendicular to megadunes. The comparisons were conducted using the albedo and temperature values and normalised using mean and standard deviation for each transect. Moreover, we determined the strength of the relationship between SPWD vs NIR albedo, and SPWD vs thermal brightness temperature (applied on the moving averages of 11 pixels weighted based on the distance from the central point) using linear regression. The comparison analysis was conducted at seasonal scale for the 2013-2014 (4 images) and at pluriannual scale on 17 images distributed over 8 years.

After having visually identified the thresholds of SPWD, NIR albedo and thermal brightness temperature on the image from 17/Dec/2015, which was one of the best available images in terms of cloud cover (~0%) and presenting no blowing snow/fog and the lowest SZA (67°) for the EAIIST site, we applied a conditional calculation to automatically map glazed snow. In order to better define the detection method and evaluate the use of each parameter, we first applied the automatic detection on the entire tile of Landsat (path 69, row 119; ~36,000 km^2) and then on a narrower area (~2,400 km^2), which showed higher homogeneity in NIR and TIRS 1 bands. Different thresholds of NIR albedo and thermal brightness temperature were used, which allowed the detection of the highest amount of glazed snow surface in the entire analysed area. The thresholds were defined as follows: NIR albedo < 0.82 and thermal brightness temperature > 246.5 K on the entire tile and NIR albedo < 0.805 and thermal brightness temperature > 247.6 K on the narrower area. Additionally, to determine the role of the SPWD in the automatic detection, we performed the classification by first excluding and then including this parameter (SPWD > 1 m km^{-1}).

2.2.42 Megadune movement estimation

~~Megadune morphology advances windward whereas the ice flows downhill; the two processes present different directions and modules (Frezzotti et al., 2002a).~~

~~By using different images and available data on megadune fields, we are thus~~ Frezzotti et al. (2002b) pointed out that the megadune migration and ice sheet surface flow show a similar intensity but opposite directions, difference between topographic slope and SPWD.

By using different satellite images and field data, we are able to provide megadune migration components: ice-flow (*If*) direction, which is correlated to topographic slope, sedimentological migration (M_s), caused by sedimentological process linked to deposition (on the upstream dune flank) and ablation (on the downstream dune flank) of snow, and the result of these processes, the absolute migration (M_a):

$$\overrightarrow{M_a} = \overrightarrow{M_s} + \overrightarrow{If} \quad (5\text{~~5~~}1)$$

During the 1998-99 It-ITASE traverse, at the D6 site (75° 26’ 53’’ S, 129° 49’ 39’’ E) an ice velocity of 1.46±0.04 m s^{-1} with an aspect of 97°(Vittuari et al., 2004) was measured using Global Positioning System (GPS) (It-ITASE site, Fig.3a).

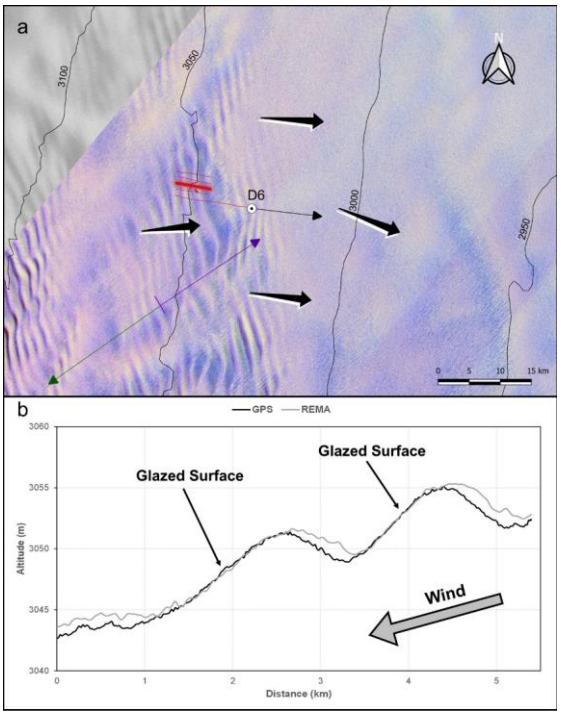

Figure 3: a) Location of the transects (red) at the It-ITASE site. False colour Landsat image and RAMP Radarsat Mosaic (Jezek, 1999) in background, black arrows as ice-flow (MEaSUREs and D6 site), purple arrow as wind direction from sastrugi and green arrow as dune absolute migration. Universal Transverse Mercator (UTM) projection. b) Topographic section of two megadunes (red highlighted transect in a), with the black line representing elevation from in situ GPS observations (1999) and grey line from REMA DEM (2014).

Additionally, during this traverse, megadunes were surveyed by means of GPS and Ground Penetrating Radar (GPR)GPR-GPS to measure theice velocity, surface elevation and internal layering of present and buried megadunes; we. We compared these measurements with the REMA DEM derived by satellite images acquired in 2014 to estimate the sedimentological migration of the megadunes. To estimate the absolute megadune migration, we used Landsat 8 OLI imagery, in particular its panchromatic band (B8), with a spatial resolution of 15 m, and Sentinel-2 imagery (Band 8 NIR) at 10 m spatial resolution.

We considered the widest temporal interval between two cloud-free images of Landsat 8 / Sentinel-2, that were in a similar period of the year, in order to avoid relevant differences in the SZA that could confound the feature tracking algorithm. We identified three pairs of images per area, subdivided in four Landsat pairs and two Sentinel pairs (Table 1).

Zone	Satellite	t_0	t_1	t span (a)	Mean M_a ($m\ a^{-1}$)	STD M_a ($m\ a^{-1}$)	Yearly ERR M_a ($m\ a^{-1}$)	Features
It-ITASE	L8	02-Dec-2014	30-Nov-2019	5	14.0	3.9	2.6	30073
It-ITASE	L8	02-Dec-2014	02-Dec-2020	6	12.8	3.4	2.5	30538
It-ITASE	S2	13-Dec-2016	27-Dec-2020	4	11.4	3.8	1.7	537304
EAIIST	L8	27-Dec-2013	28-Dec-2019	6	11.9	3.6	8.9	316951
EAIIST	L8	17-Dec-2015	30-Dec-2020	5	14.2	3.4	16.3	139622
EAIIST	S2	10-Jan-2018	02-Jan-2021	3	10.5	4.1	11.7	1329648

Table 1. Results of the absolute migration of megadunes calculated from IMCORR based on Landsat 8 OLI (L8) and Sentinel-2 (S2) imagery at the It-ITASE and EAIIST sites.

In addition, we tried performing a long-term analysis, comparing Landsat 7 ETM+ imagery against Landsat 8 OLI (Table A1). The time span is respectively for the two areas as follows: 29-Dec-1999 / 27-Dec-2013 and 29-Dec-1999 / 28-Dec-2019 (EAIIST), and 02-Jan-2000 / 06-Jan-2016 and 02-Jan-2000 / 17-Jan-2020 (It-ITASE). In fact, even if the co-registration error could be higher for these images as they were acquired from different satellites, the errors should be mitigated by using image pairs acquired from the same path/row in a similar period (i.e. same incidence angle), so that most of the uncertainty arising from both sources cancel out when measuring displacement (Jeong and Howat, 2015).

With the aim of calculating the superficialsurface velocity and direction of megadunesmegadune movement, the feature tracking module *IMCORR* (Fahnestock et al., 1992; Scambos et al., 1992)(Fahnestock et al., 1992; Scambos et al., 1992) was run in *System for Automated Geoscientific Analyses* (SAGA GIS.). This algorithm performs image correlation based on two images providing the displacement of each pixel between the second and first image (Jawak et al., 2018).(Jawak et al., 2018). Prior to feature tracking, each image pair was pre-processed by using a low pass filter with a length scale of 150 m implemented through a Fast Fourier Transform to smooth out the sastrugi and leave megadune features for tracking. Finally, by dividing the displacement values obtained through IMCORR by the corresponding time period, we obtained the absolute migration of the megadunes in m a^{-1}.

For comparison with the previous results, we also employed another method to evaluate the megadune migration. By using Landsat 8 OLI imagery, similarly to what already done for the detection of sastrugi, and applying an edge detection on a FCC

~~of bands 3, 4 and 5 of Landsat 8,~~band 5 (NIR), it is possible to identify the megadune crest and trough at the edges between leeward (glazed snow) and windward (sastrugi) zones ~~of megadunes and thus the megadune ridges, since wind glazes and surrounding areas behave differently from the spectral point of view (Frezzotti et al., 2002b). To investigate variations over a period of 20 years, we used Landsat 7 ETM+ images also in this case, creating a FCC with bands 2, 3 and 4.~~. The obtained direction raster was manually cleaned from errors and artefacts (~~based on size and direction~~angles < 200° and > 240°, intensity < 5 m a^{-1}), and then vectorized after ~~a~~ thinning ~~step.~~, i.e., reducing the number of cells used to represent the width of the features to 1 pixel. Comparing the obtained velocity fields in different years, we could observe the absolute migration of the ~~dunes. The results from IMCORR and GPS observations were compared with the *MEaSUREs ice-flow velocity* product (Rignot et al., 2017), that provides the highest-resolution (450 m) digital mosaics of ice motion in Antarctica (assembled from multiple satellite interferometric synthetic-aperture radar systems, mostly between 2007-2009 and 2013-2016), showing for each pixel the direction and the velocity of ice flow.~~ megadunes.

We considered the widest temporal interval between two pairs of cloud-free images of Landsat 8 (4 pairs) and Sentinel-2 (2 pairs), that were in a similar period of the year, to avoid relevant differences in the SZA that could confound the feature tracking algorithm (Table 1).

Zone	Satellite	t_0	t_1	t span (a)	Mean M_a (m a^{-1})	STD M_a (m a^{-1})	Features
It-ITASE	L8	02-Dec-2014	30-Nov-2019	5	14.0	3.9	30073
It-ITASE	L8	02-Dec-2014	02-Dec-2020	6	12.8	3.4	30538
It-ITASE	S2	13-Dec-2016	27-Dec-2020	4	11.4	3.8	537304
EAIIST	L8	27-Dec-2013	28-Dec-2019	6	11.9	3.6	316951
EAIIST	L8	17-Dec-2015	30-Dec-2020	5	14.2	3.4	139622
EAIIST	S2	10-Jan-2018	02-Jan-2021	3	10.5	4.1	1329648

Table 1. Results of the absolute migration of megadunes calculated from IMCORR based on Landsat 8 OLI (L8) and Sentinel-2 (S2) imagery at the It-ITASE and EAIIST sites.

The results from IMCORR and GPS observations were compared with the *MEaSUREs ice-flow velocity* product (Rignot et al., 2017), that provides the highest-resolution (450 m) digital mosaic of ice motion in Antarctica (assembled from multiple satellite interferometric synthetic-aperture radar systems, mostly between 2007-2009 and 2013-2016), showing for each pixel the direction and the velocity of ice flow with a mean error of 3-4%.

3 Results

3.1 ~~NIR~~ Megadune characterization and ~~broadband albedo~~automatic detection

~~As an initial approach to the spectral analysis of megadune fields, we evaluated its response in the NIR part of the spectrum (OLI Band 5), because it is in such wavelengths that major differences between snow and ice are found (Warren, 1982). Glazed surfaces show an intermediate spectral reflectance between snow and ice (Frezzotti et al., 2002a; Scambos et al., 2012) and thus are easier to detect in the NIR than at visible wavelengths.~~

~~We first focused on an intra seasonal analysis of NIR albedo, using 4 scenes between November and January 2013-2014. A general pattern of NIR albedo is detected (see Fig.4a), with higher values in the upwind area and lower ones downwind.~~

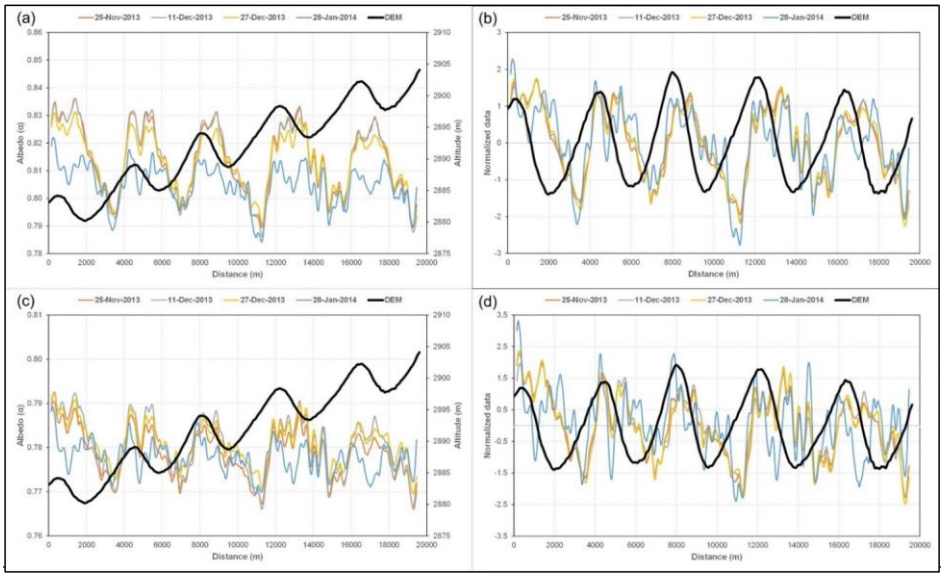

~~**Figure 4: NIR (a-b) and broadband albedo (c-d) during the austral summer season 2013-2014 for transect C at the EAIIST site (see Fig.2 for location) and elevation from REMA DEM. a and c represent the moving average of 11 pixels and b-d the normalized moving average (with detrended topography).**~~

~~In particular, 25-Nov-2013, 11-Dec-2013 and 27-Dec-2013 show a very similar pattern along all the transects and only 28-Jan-2014 diverges from it, with a smaller difference between maximum and minimum values. However, the main tendency is maintained. This small difference could depend on the different SZA between the scenes. In fact, increasing the SZA, a major~~

heterogeneity was found in both study areas, because of an exponential effect on albedo values, as suggested by Picard et al. (2016). The first three scenes present a small range of SZA, between 67° and 69°. In contrast, the last scene has a higher SZA of 72°. This discrepancy between scenes with SZA < 70° and > 70° is constant for all the seven analysed transects, which have different wind directions (35°-63°, Fig.2). On average, in the central transect of the Landsat scene (transect C), the albedo of glazed surface is lower by 0.03-0.04 compared to the upwind zone of the dunes, from a NIR albedo range of 0.81-0.84 in the upwind area (snow sastrugi) to a 0.77-0.81 range downwind (glazed surface).

Looking at broadband albedo (Fig.4b), the dominant pattern seen for NIR albedo is still present and again the main intra-annual difference is observed between January and the other scenes. In general, broadband albedo values show lower variability compared to NIR albedo and their range is lower. The highest values, located on the upwind part of the dune, range between 0.78-0.80 while on the downwind areas we found an average albedo of 0.77-0.78. On average, the difference between snow (upwind) and glazed surfaces (downwind) is around 0.02, almost halved compared to NIR albedo. The difference in the detection ability of NIR and broadband albedo stems from the fact that broadband albedo obtained by using Liang conversion algorithm (Liang, 2001) considers the visible area of the spectrum and the shortwave infrared. Considering the LL transect (Fig.2), from broadband albedo it is hardly possible to recognize the differences between glazed and non-glazed areas, which in the visible wavelengths look very similar (Warren, 1982). Nevertheless, in other parts of the Landsat scene, e.g., LR transect (Fig.2), downwind and upwind areas of the dunes are easily detected, with an albedo difference higher than 0.02.

Focusing on the interannual analysis of the 14 available scenes in the EAHST area (Table A1), we chose to divide the dataset into two sub-datasets in accordance with the SZA values of each single date, following the reasons previously discussed (Picard et al., 2016). The first sub-dataset considered those scenes with a SZA < 70° and the second one with SZA > 70°.

In Fig.A1, we show four NIR albedo graphs of the scene centre transect (C) considering the 7-scene dataset from 2013-2019. Looking at Fig.A1b-d the differences between the scenes with SZA < 70° and SZA > 70° become evident; in fact, while the former shows a strong homogeneity among the different images, the latter are more heterogeneous. Above all, NIR albedo on 14-Oct-2015 diverges from all other observations, owing to its very high SZA of 81°. In general, excluding 14-Oct-2015, all the scenes show the same pattern, with higher NIR albedo values in the upwind areas of the dunes and lower albedo in the downwind zones, characterized by the presence of glazed surfaces (Fahnestock et al., 2000; Frezzotti et al., 2002a, b), as already observed in the intra-annual analysis. However, strong differences between different summer seasons are not detected, and the albedo pattern remains fairly constant.

3.2 Brightness temperature

The TOA brightness temperature was here calculated form Band 10 (10.60-11.19 μm) and 11 (11.50-12.51μm) of Landsat 8. Temporally, for both bands we observed an intra-seasonal trend: in fact, while brightness temperature remains ≥ 244K (-29° C)On average, in the 5 analysed transects NIR albedo ranges from 0.81 to 0.86 (α) in the upwind area (snow sastrugi) and from 0.73 to 0.81 (α) downwind (glazed surfaces), with differences inside the transects of about 0.07 (α) with a maximum

value of 0.1 (α). The maximum contrast of NIR albedo between glazed surfaces and snow sastrugi usually occurs at springtime (October-November) and decreases during the summer season (Fig. 2). Our remote sensing observations agree with previous analysis that pointed out that in late summer, radiative cooling of the uppermost surface layer leads to formation of a surface frost, by condensation of local atmospheric vapour onto the snow surface; this gives the glazed surface a more diffuse specular reflection than in spring and changes its appearance in albedo and brightness temperature (Scambos et al., 2012 and references therein). Along the transects, the correlation of NIR albedo from the different images is high (R^2 up to 0.99) during the spring season (24 Nov 2013, 27 Dic 2013) and decreases by the end of the summer and in comparison with the following years, with an R^2 of 0.7 only after 2 years (17 Dec 2015) and up to 0.6 after 6 years (Dec 2019). A Similar decrease in correlation occurs from the comparison of the SPWD and NIR albedo from 2013 (R^2 0.66) to 2019 (R^2 0.39).

For the thermal brightness temperature, we observed an intra-seasonal trend on all transects: in fact, while thermal brightness temperature remains ≥ 244 K during the middle of the summer (11-Dec-2013 and 27-Dec-2013), it decreases moving away from the summer solstice. Temperatures range between 238 K and ~~241 K (-35 / -32° C)~~240.5 K on 25-Nov-2013, 26 days from the solstice. The difference increases on the date farthest ~~date~~from the solstice, 28-Jan-2014 (38 days~~)~~ from the solstice), with the lowest values ranging between 236 K and 239 K ~~(-37 / -34° C). Looking at the 5 transects, we found the same pattern previously observed for the albedo, but proportionally inverse with respect to topography, in both Band 10 (Fig.5a) and 11 (Fig.5b).~~

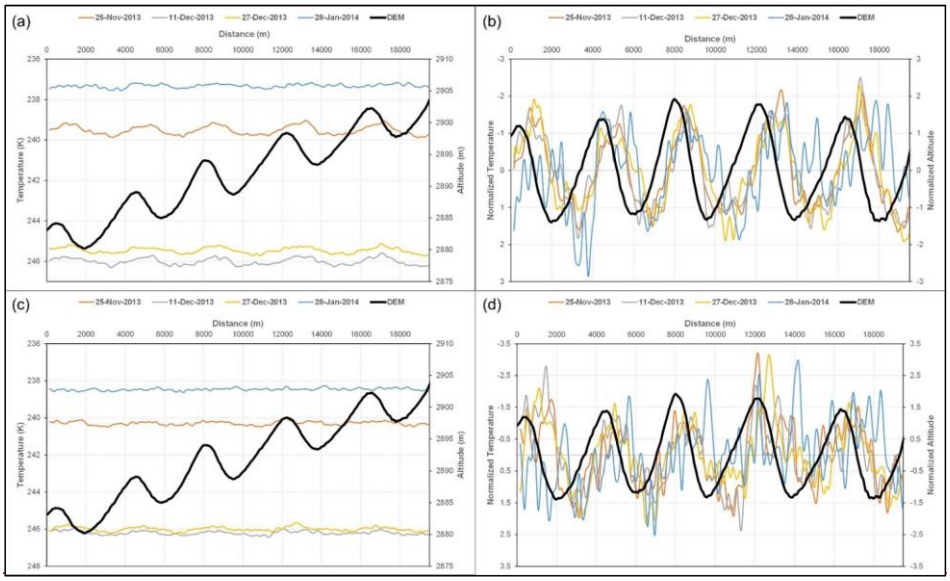

~~**Figure 5: Thermal infrared Band 10 (a-b) and 11 (c-d) in the austral summer season 2013-2014 for the C transect (see Fig. 2 for location) and elevation from REMA DEM. a-c represent the weighted moving averages based on 11 transect pixels and b-d the normalized moving averages (with detrended topography).**~~

~~In fact, higher temperatures correspond to the glazed part of downwind areas of the dunes and conversely, lower values are related to snow sastrugi in the upwind zones, in accordance with Fujii et al. (1987). In general, Band 11 is noisier compared to Band 10, even if the general pattern can still be detected.~~

~~Nevertheless, in comparison with spectral and broadband albedo observations, here the differences between downwind and upwind faces are very small, around 1 K at maximum and are more evident in Landsat 8 OLI Band 10. These differences are directly correlated to the ones observed in albedo, as a higher quantity of energy is absorbed on glazed surfaces. High correlations are also found between NIR albedo and.~~ The brightness temperature ~~(e.g., R = 0.85 with Band 10 in transect C).~~varies up to 1.5 K for each transect, but up to 3-4 K within individual images. Intra-annually, the difference between glazed surfaces and snow is higher ~~at~~during the ~~end of~~ spring (max 1 K in November) and tends to decrease over time, becoming lower than 0.5 K at the end of summer~~,~~ (January), where differences between the two surfaces are hardly detectable~~.~~ and the correlation between the two parameters frequently decreases drastically. These differences are directly correlated to the ones observed in NIR albedo, as a higher quantity of energy is absorbed on glazed surfaces.

3.3 Topographic aspect and slope, wind direction and SPWD

The two study areas, It-ITASE and EAIIST, are in a sloping zone, where, respectively, the altitude increases moving E-W, while the elevation ranges from 2700 to 3200 m in both areas. Thus, the topographic aspect (the direction that a topographic slope faces) is generally E (~ 90°, It-ITASE and ~ 80°, EAIIST), including the leeward part of the megadunes with glazed surfaces, and only the windward section faces W (topographic aspect ~ 270°, It-ITASE and ~ 260°, EAIIST). As regards the topographic slope at a 10 km scale, it is on average 1.5 m km^{-1} and 1.8 m km^{-1} for the It-ITASE and EAIIST areas.

In order to analyse the regional wind direction over the study area, we used ERA5 and sastrugi-based wind direction retrieved from Landsat 8 OLI (Table 2).

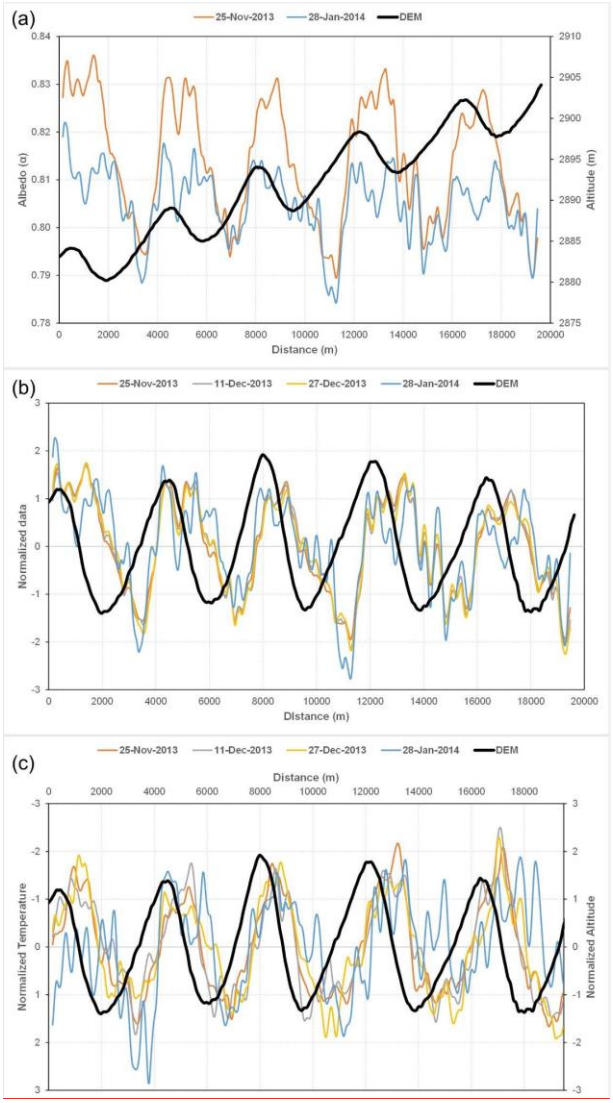
(a)
25-Nov-2013
28-Jan-2014
DEM
Albedo (α)
Altitude (m)
Distance (m)
(b)
25-Nov-2013
11-Dec-2013
27-Dec-2013
28-Jan-2014
DEM
Normalized data
Distance (m)
(c)
25-Nov-2013
11-Dec-2013
27-Dec-2013
28-Jan-2014
DEM
Distance (m)
Normalized Temperature
Normalized Altitude

Figure 2: (a) moving average (based on 11 transect pixels) of NIR albedo (α) between November 2013 and February 2014 for transect C at the EAIIST site (see Fig. 1c for location) and elevation from REMA DEM. Corresponding normalised moving average of NIR albedo (b) and thermal brightness temperature TIRS1 (c) during the austral summer season 2013-2014 for transect C and elevation from REMA DEM (detrended topography).

High correlations are found between NIR albedo and thermal brightness temperature with a R^2 up to 0.67 (95% confidence interval) and between SPWD versus NIR albedo and thermal brightness temperature (R^2 = 0.44 and 0.57 at 95% confidence interval, respectively) calculated along all the transects (Fig. 3). The comparison between thermal brightness temperature and SPWD shows the same pattern observed for the NIR albedo, but proportionally inverse with respect to SPWD (Fig. 3), with higher temperatures corresponding to the glazed part of downwind areas of the dunes and conversely, lower values related to snow sastrugi in the upwind zones, in accordance with previous authors (e.g., Fujii et al., 1987; Scambos et al., 2012).

On the basis of the transect observations, the highest variabilities in NIR albedo and thermal brightness temperature at seasonal (spring-summer) to pluriannual scale is observed in the snow accumulation area on the upwind flank and the bottom of the leeward flank (Fig. 2), whereas the glazed surface NIR albedo and thermal brightness temperature remain more stable and more highly correlated at seasonal (spring-summer) and pluriannual scale.

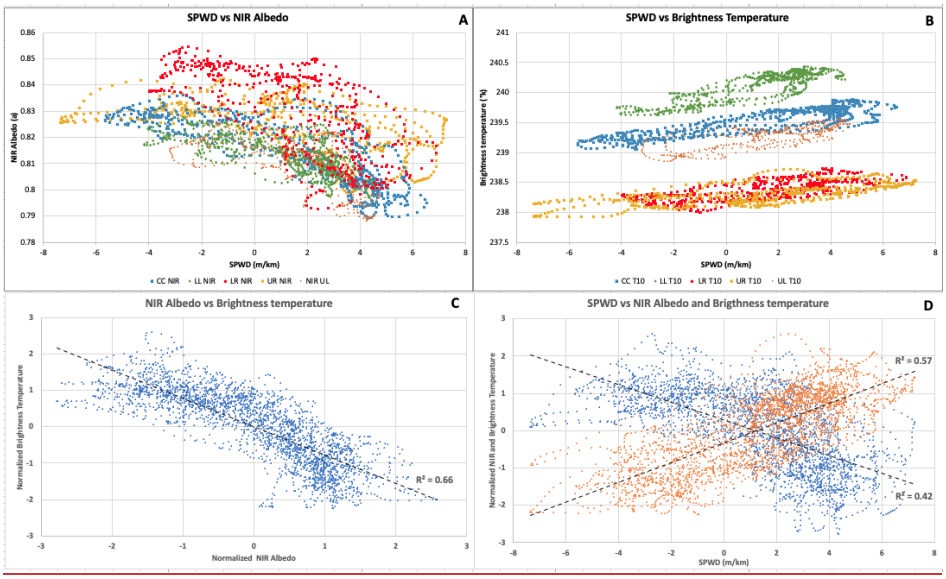

Figure 3: Diagram plots of transects at the EAIIST site from a Landsat 8 image acquired on 25-Nov-2013: (A) SPWD (slope along the prevailing wind direction) compared within each transect (C, LL, LR, UL, UR; Fig. 1 for location) with NIR spectral albedo and

(B) thermal brightness temperature; (C) normalised NIR albedo of all transects compared with brightness temperature with linear regression; (D) SPWD compared with normalised NIR albedo and thermal brightness temperature for all transects with linear regression.

The analysis of sastrugi direction using 7 Landsat scenes from the spring and summer months during the period 2013-2020 show small differences in direction within each image and in repeated imagery (< 5°), confirming the stability in direction of sastrugi landforms and thus the persistence of katabatic wind.

The comparison of the results of wind direction obtained using sastrugi direction by satellite (resampled using bilinear interpolation) and ERA5 present similar values for both areas, with lower difference in the EAIIST area (differences of 1° in average values) compared to It-ITASE (9-14°, see Table A3).

At the regional scale (30 km spatial resolution), the entire megadune field has an average SPWD of 1.2 m km^{-1}, when calculated using sastrugi-based wind direction, and 1.1 m km^{1} when using ERA5, in agreement with previous studies (e.g., Frezzotti et al., 2002b). To distinguish between leeward (glazed surface) and windward flanks of the dunes for the two sites, the SPWD based on sastrugi was further resampled to 120 m using bilinear interpolation. For the SPWD on megadunes, we found a mean value of 5.6±1.0 m km^{-1} for the leeward side and negative SPWD values, with a mean of -4.2±1.6 m km^{-1} on the windward flanks.

Applying the automatic detection on the entire Landsat scene from 17-Dec-2015, when excluding the SPWD, approximately 34% of the entire tile was detected as glazed snow, compared to 24% using also SPWD. On the smaller area instead, a slight variation was detected with and without SPWD (22% and 23% respectively). Clipping the glazed snow surface estimated on the entire Landsat 8 tile by using the tile-based thresholds to the extent of the narrower area, an overestimation of 70% was found in comparison with the results obtained directly on the smaller area with the area-specific thresholds and when using the SPWD, rising to +88% without SPWD (Fig. 4).

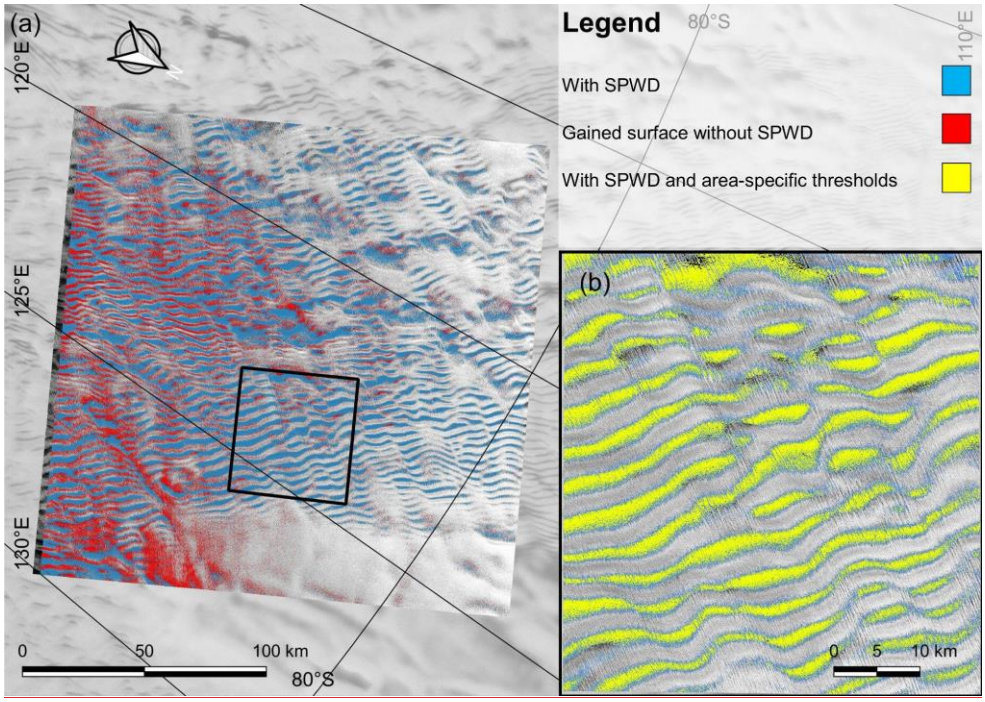

Figure 4: (a) wind-glazed surface automatic detection at the EAIIST site with the inclusion of an SPWD threshold in blue, and the overestimated detected surface when no SPWD was used. (b) the sample narrow area with thresholds defined on the entire tile of Landsat for NIR albedo and thermal brightness temperature (blue) and with thresholds defined on the smaller area (yellow).

3.2 Megadune migration

The absolute megadune movement calculated using feature tracking on optical satellite image pairs spans from 3 to 6 years and presents small differences in the two study areas, ranging between 10.5 m a^{-1} and 14.2 m a^{-1} overall, with no detected significant trends over time. The average values are similar when using different datasets (Landsat 8 OLI and Sentinel-2), but with Sentinel-2 velocities showing slightly lower average values compared to Landsat 8. Moreover, due to the slightly higher spatial resolution (10 m versus 15 m), the number of features tracked using Sentinel-2 are an order of magnitude higher than those of Landsat 8 OLI (Table 1). The direction of the migration does not differ much across the different datasets, showing opposite values with respect to wind direction. The second method used to calculate the migration velocity is the ridge

vectorization and tracking for the same image pairs. This method shows slightly higher velocities (16.7±3 m a^{-1}) than IMCORR tracking of megadune features (11.9±3.6 m a^{-1}) at the EAIIST site for the period 2013-2019, but within the error.

At the Dataset	Average	Max	Min	Dataset	Average	Max	Min
Landsat 8	224°	232°	212°	Landsat 8	240°	250°	215°
ERA5 ≥ 0m/s	225°	230°	220°	ERA5 ≥ 0m/s	227°	236°	215°
ERA5 ≥ 3m/s	225°	229°	220°	ERA5 ≥ 3m/s	226°	233°	217°
ERA5 ≥ 5m/s	225°	229°	220°	ERA5 ≥ 5m/s	226°	234°	217°
ERA5 ≥ 7m/s	225°	235°	220°	ERA5 ≥ 7m/s	227°	236°	218°
ERA5 ≥11m/s	223°	229°	216°	ERA5 ≥11m/s	231°	240°	223°

Table 2. wind direction statistics (average, maximum and minimum values) for the considered datasets: Landsat 8 at 30 m spatial resolution and ERA5 at 30 km spatial resolution (divided into 5 sub-datasets according to wind speed) at the EAIIST site (left) and It-ITASE (right).

Concerning the It-ITASE area, ERA5 shows an average meteorological wind direction (direction from where the wind blows) of 227±4°, whereas an average of 240±6° was calculated from the sastrugi. In the EAIIST area, the difference is lower, with a mean of 225±2° from ERA5 and 221±4° based on the sastrugi. The small difference between the two datasets is certainly caused by the fact that the formation of sastrugi is linked to katabatic wind erosion processes (Table 2), and thus represents the direction of high-speed winds. The difference between the average wind direction calculated from ERA5 and Landsat is rather low and, in fact, becomes even lower (from 4° to 2° and from 13° to 9° in EAIIST and It-ITASE sites respectively) considering a higher wind speed (≥ 11 m s^{-1}). In addition, this discrepancy could be caused by the different spatial and temporal resolutions between the two datasets (30 m vs 30 km, scene-based vs average of 20 years).

Owing to these small differences, the SPWD is the same when using ERA5 or sastrugi-based wind direction, because the SPWD algorithm considers 8 possible aspect classes. At the regional scale (30 km spatial resolution), the entire megadune field (almost 500,000 km^2 area) which covers the two study sites, has an average SPWD of 1.2 m km^{-1}, which is in accordance with previous studies (e.g., Frezzotti et al., 2002b). To distinguish between leeward (glazed surface) and windward flanks of the dunes for the two sites (i.e., EAIIST and It-ITASE), the SPWD based on sastrugi was further resampled to 120 m and thresholds were determined using the 30 sample polygons. For the leeward side of the dunes, a mean SPWD of 5.1±1.2 m km^{-1} was calculated. In contrast, the windward flanks show negative SPWD values, with a mean of -4.3±1.7 m km^{-1} (Fig.3a).

3.4 Correlations between albedo, SPWD and brightness temperature

From albedo (both broadband and NIR spectral), brightness temperatures and SPWD, we estimated the correlation coefficients (R) between optical and topographic measures along the transects. Focusing for example on a scene showing one of the lowest

relative SZA (e.g., 27-Dec-2013, EAIIST scene, SZA = 67°), chosen to minimize possible errors in the albedo, we discovered a high average R for all the transects for each of the considered parameters. Concerning the albedo, NIR α showed higher |R| values in relationship with the SPWD, averaging -0.60, compared to broadband albedo, whose R decreases to -0.35. Brightness temperature showed much better statistics, with an average of 0.76 and 0.71, for band 10 and 11 of Landsat 8 OLI, respectively. In detail, taking into consideration the transect (C), which shows the best statistics, the R for broadband albedo, NIR spectral albedo and Thermal bands 10-11 was respectively: -0.64, -0.78, 0.87 and 0.77. These high correlation coefficients are easily observable also looking at the plots that compare the SPWD with albedo and brightness temperature (Fig.6).

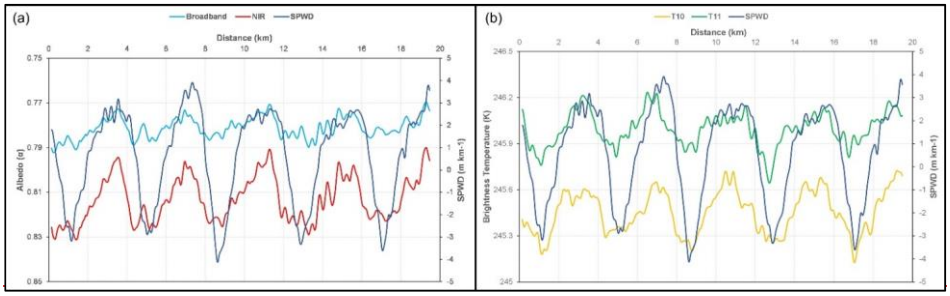

Figure 6: Transect C plots of SPWD (slope along the prevailing wind direction) at the EAIIST site (Fig. 2 for location), compared to broadband and NIR spectral albedo (a) and brightness temperature from Thermal bands 10 and 11 of Landsat satellite (b) on 27-Dec-2013 (SZA = 67°).

3.5 Megadune classification and temporal variability

By employing SPWD, albedo and brightness temperature, we performed a classification of the megadune field with the aim of detecting and mapping the downwind (glazed surfaces) and upwind flanks of the dunes. In detail, as NIR spectral albedo and brightness temperature from band 10 provided the best R statistic with SPWD and showed the highest differences between the sides of the megadunes, we applied a classification of the areas based on these 3 features. Focusing on an area of the EAIIST site, which is characterized by wide megadune presence, we provide an intra-annual and inter-annual analysis of glazed surfaces between 2013 and 2020 (Fig.7).

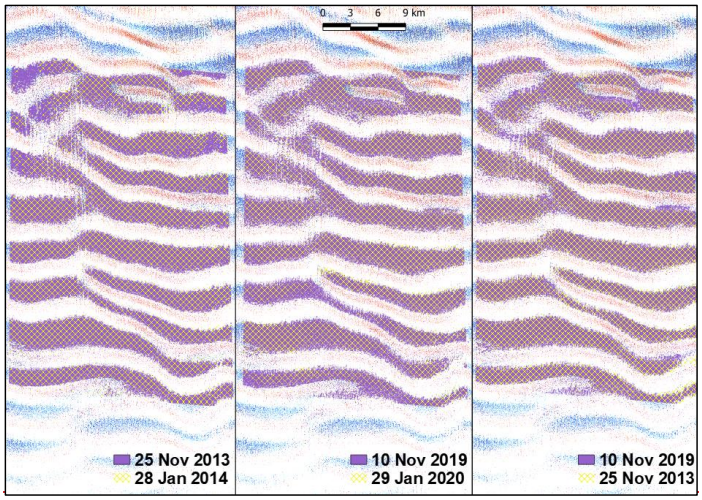

~~**Figure 7: Wind glazed surface variations in the 2013-2014 and 2019-2020 summer seasons in a sample polygon at the EAIIST site (location in Fig.2a).**~~

~~Only two summer seasons (the first one, 2013/14 and the last one, 2019/20) allowed a complete temporal coverage, from the late spring (November) to the end of summer (January) and in both cases we detected a decrease in the glazed surface between November and January. In these two summers, the coverage of glazed areas decreased by 16%. Inter-annually, contrasting results were obtained comparing the dates of January (2014 and 2020) and November (2013 and 2019). In fact, a much higher increase in area was observed using January scenes, almost 1% (≈0.16% per year) against 0.24% using November scenes (≈0.04% per year). Fahnestock et al. (2000) pointed out that in late summer, radiative cooling of the uppermost surface layer leads to the formation of surface frost, by condensation of local atmospheric vapor onto the glazed surface with a more diffuse specular reflection than in spring, which changes its albedo and does not permit the discrimination between glazed surface and surrounding snow surface. Considering the It-ITASE and EAIIST sites in those portions included inside the main megadune field (Fig.1), we have around 20,500 km^2 and 33,000 km^2 of megadune coverage in the two areas respectively, calculated using huge megadune polygons by (Fahnestock et al., 2000) (Fig.1). In these areas, approximately 20-25% of the surface is represented by glazed surface.~~

~~3.6 Superficial velocity analysis and upwind migration~~

~~The calculation of absolute megadune migration was carried out by using feature tracking and by comparing megadune ridges detected on two dates. Regarding the first method, two intra-sensor analyses of Landsat 8 OLI and Sentinel-2 were performed~~

~~(Table 1). In It-ITASE area, the migration ranges between 11.5±3.8 m a^{-1} (242±12°) for Dec-2016 / Dec-2020 and 14±3.9 m a^{-1} (241±11° direction) for Dec-2014 / Nov-2019. At the other site, EAIIST, a slightly higher heterogeneity was found, as values range between 10.5±4.1 m a^{-1} (219±11°) for Jan-2018 / Jan-2021 and 14.3±3.4 m a^{-1} (225±10°) for Dec-2015 / Dec-2020. The inter-sensor approach using Landsat 7 ETM+ and 8 OLI shows generally lower values (<10 m a^{-1}) at both sites, but with an uncertainty estimated by IMCORR higher than the annual velocities, i.e., 21 m a^{-1} on average, which suggests that these results are not statistically robust. In both study areas the migration calculated from Sentinel-2 imagery shows on average a lower velocity compared to Landsat (11.4±3.8 m a^{-1} and 10.5±4.1 m a^{-1} respectively for It-ITASE and EAIIST, Table 1), even if the direction remains similar. At the same time, these results are supported by a larger number of calculated features (an order of magnitude higher), and the higher spatial resolution of Sentinel-2 (10 m) compared to Landsat 8 OLI (30 m). The second method, i.e., megadune ridge vectorization for the same image pairs, shows slightly higher velocities than IMCORR, e.g., 16.7±3 m a^{-1} at the EAIIST site for the period 2013-2019.~~

~~The~~ D6 It-ITASE site ~~was covered by~~, 5 GPS-GPR transects ~~along a megadune field;~~were surveyed on megadunes (Frezzotti et al., 2002b); the comparison between GPS elevations (3-Jan-1999) and REMA DEM (02-Feb-2014) provides information about the ~~sedimentological migration of~~ relative change in elevation at high resolution (decametre level) of the megadunes during the past 15 years~~, based on nine megadunes along the traverse.~~. On the 5 transects, we observe an almost stable elevation in correspondence with glazed surface/leeward flank, whereas the maximum difference in elevation (from +1.2 to +1.9 m, with an average maximum value of +1.4 m) occurs always in the snow accumulation/upwind flank on the correspondence of the trough (Fig. 5). By projecting the transects along the prevalent wind direction (239°), based on the surrounding sastrugi orientation, we were able to evaluate the megadune ~~sedimentological~~ migration ~~between GPS and DEM observations. Considering~~using the relative change in elevation. Using the crest/trough position of each dune, we calculated ~~the~~an average displacement ~~in this ≈15-year period, obtaining an average superficial speed~~ of 11±5.2 m a^{-1} from all transects (Fig.~~3b). The~~ 5). The migration of the dunes is evident in all transects with the upwind migration of the crest over the upstream ~~migration~~flank and of the ~~dunes is mostly evident~~trough on the ~~upwind flank, i.e., accumulation area, in every transect; in~~upstream flank of the previous megadune. In contrast, the glazed surfaces on the downwind flank~~, i.e., ablation part covered by glazed surfaces,~~ remained generally ~~constant~~stable in elevation over time (Fig.~~3b~~ 5) but are clearly buried at the upstream flank foot and migrate at the crest. At the D6 site, Vittuari et al. (2004) measured an ice velocity of 1.46 ±0.04 m a^{-1} with a direction of 97° using repeated GPS measurement between 1999 and 2001. The closer value of MEaSUREs ice flow at the D6 site is 2.2±1.1 m a^{-1} with a direction of 89°, in agreement with GPS measurements. At the EAIIST site, MEaSUREs data show an ice flow of 6.1±3.4 m a^{-1} with a direction of ~65°. Both velocity directions agree with the topographic slope at the site. Applying Eq. (1) for the calculation of megadune-migration components, we obtained a sedimentological migration of 18.4±6.7 m a^{-1} (229°) at EAIIST and 15.4±4.7 m a^{-1} (246°) at It-ITASE using Landsat 8 OLI data, and 16.0±7.3 m a^{-1} (230°) at EAIIST and 13.6±4.9 m a^{-1} (245°) at It-ITASE with Sentinel-2.

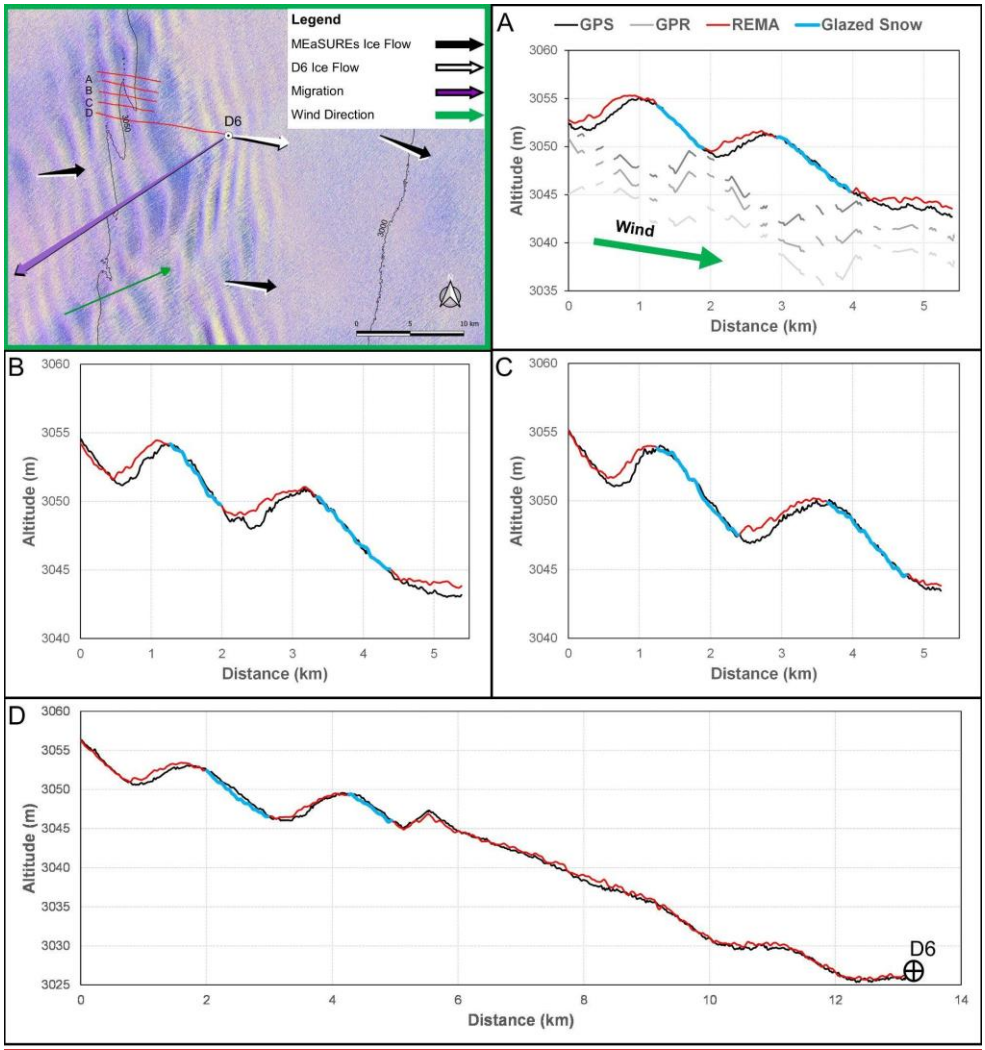

Figure 5: Location of the GPS transects (red) at the It-ITASE site with false colour Landsat 8 OLI image in background (18/Dec/2014). Universal Transverse Mercator (UTM) projection. Topographic section of four transects (A-B-C-D), with the black

lines representing elevation from in situ GPS observations (1999), red lines from REMA DEM (2014) and blue lines as glazed snow detected by Landsat image on 18-Dec-2014. In (A) we also show three GPR internal layering palaeo-megadunes acquired during the It-ITASE traverse in grey shades (Frezzotti et al., 2002b).

4 Discussion

~~4.1 Wind and SPWD differences and correlations~~

~~At both investigated sites, the direction of the wind from ERA5 at velocity higher than 11 m s^{-1} was found to be closer to the direction of sastrugi surveyed by satellite. This high speed was previously reported by Kodama et al. (1985) and Wendler et al. (1993) to be required for the formation of sastrugi. In fact, calculating the wind direction based on sastrugi orientation, we generally obtained values slightly different from the ones obtained from ERA5 (Hersbach et al., 2020) considering all wind velocity values. Even if the EAIIST site shows similar average directions, i.e., 221° based on sastrugi and 225° from ERA-5, respectively, in the other study area (It-ITASE) a slightly worse agreement is observed, with difference in the average values of 12° (239° for sastrugi-based directions and 227° for ERA-5). However, (Frezzotti et al., 2002b) pointed out that at the it-ITASE site the sastrugi direction (220° – 225°) measured on the field in 1998-1999 is parallel to the sastrugi-glazed surface field inferred by Landsat 7 ETM+ satellite image recorded in 2000 (230° – 235°). The observed differences can be caused by a number of reasons, including spatial resolution (30 km for ERA-5 compared to 30 m for Landsat). Further still, for geomorphological reasons the direction retrieved from Landsat is strongly dependent on prevailing winds (katabatic winds), that shape the sastrugi, while ERA5 also takes into account other wind directions than the katabatic. Thus, looking at Table 2, it is evident how higher wind speeds from ERA5, especially ≥ 11 m s^{-1}, correspond to wind directions closer to the ones obtained from sastrugi. Nevertheless, the differences between wind direction from ERA5 and sastrugi are low enough to produce an identical SPWD. In fact, with angles in the range 212°-250° (EAIIST minimum and It-ITASE maximum respectively), all the directions considered in this study, both ERA and sastrugi head towards the SW pixel (202.5°-247.5°) in the SPWD algorithm, with the exception of a few pixels at It-ITASE which show a W direction (angles between 247.5° and 250°). However, with the aim of applying this methodology at large-scale using ERA5 data, e.g., the whole continent, the differences between the two sources can be significant (e.g., at the It-ITASE site), and could produce errors in the SPWD calculation. Therefore, some verifications would be necessary, above all in those areas of Antarctica where forecast observations are missing.~~

~~4.2 Roles of albedo, brightness temperature and SPWD to map megadunes and glazed surfaces~~

~~Considering that albedo and brightness temperature are not reliable enough for megadune mapping, as unique thresholds cannot be identified to discriminate between glazed surfaces and surrounding snow, the accurate calculation of SPWD is necessary. As showed in Sect. 3.5, it would be possible to detect and properly map glazed surfaces on the leeward flank of megadunes by combining these three parameters, i.e.: SPWD, NIR albedo and brightness temperature,~~

~~allowing to study their evolution and trends over time. The SPWD is the only parameter that could be considered as "constant" at 10s km scale, considering~~**4.1 Application of the automatic detection of glazed snow on megadune fields**

The satellite derived NIR and thermal brightness temperature show large variability inside the same satellite images, in particular for thermal brightness temperature, but strong correlation among the two parameters up to a R^2 of 0.99 along each transect. The observed variabilities could be related to the different illumination condition and meteorological conditions with development of surface hoar crystal due to fog and under calm sunny weather with a downward as well as an upward vapour source to the near-surface layer. The growth of surface hoar crystals dramatically changes the snow structure, specific surface area, and density, as well as surface roughness, leading to significant changes in albedo and therefore surface temperature (Gallet et al., 2014). For these reasons, different thresholds can be required when investigating an entire tile of Landsat and a narrower area. The results from our analysis suggested the presence of a significant overestimation (at least +70%) when using thresholds defined on the entire tile and then when considering a finer scale. Nevertheless, the use of the SPWD in the automatic detection, which was possible on 17-Dec-2015 scene as the migration of megadunes in less than an year (~2016, REMA and Landsat acquisition) was lower than the spatial resolution of the used images (~10 m a^{-1} vs 30 m respectively), provided better results when considering large areas (10% of overestimation when no SPWD was used), even if its inclusion appeared not so relevant in narrower areas (1% difference with and without SPWD).

In this study, we showed the possibility to calculate the SPWD based on wind direction from ERA5 and Landsat-derived sastrugi. At both investigated sites, the direction of the wind from ERA5 at velocity higher than 11 m s^{-1} was found to be closer to the direction of sastrugi surveyed by satellite. The small difference between the two datasets could be correlated to the formation of sastrugi that is due to wind erosion processes linked to the katabatic high-speed winds, as indeed closer values are detected comparing sastrugi-based with high wind speed ($\geq$ 11 m s^{-1}) from ERA5. This high speed was previously reported by Kodama et al. (1985) and Wendler et al. (1993) to be required for the formation of sastrugi. While the EAIIST site shows similar average directions, i.e., 221° based on sastrugi and 225° from ERA5, in the other study area (It-ITASE) a slightly higher difference was found between the two datasets for wind velocity slower than 11 m s^{-1}, reaching 13° (average 240°, max 250° minimum 215° for sastrugi-based directions and average 227°, max 263° minimum 215° for ERA5). At the D6 It-ITASE site, Frezzotti et al. (2002b) pointed out that the sastrugi direction (220° – 225°) measured on the field in 1998-1999 is similar (10° difference) to the sastrugi direction inferred by Landsat 7 ETM+ satellite image recorded in 2000 (230° – 235°), similar to the difference observed between ERA5 and sastrugi detection by satellite in this study. The direction retrieved from Landsat is strongly dependent on high velocity prevailing winds (katabatic winds), that shape the sastrugi and direction, while ERA5 also takes into account other wind directions than the katabatic. In addition, this difference could be caused by the different spatial and temporal resolutions between the satellite and ERA5 (30 m vs 30 km, scene-based vs average of 20 years), as well as inaccuracies in the ERA5 wind direction. The It-ITASE site shows a larger difference in wind direction using the various datasets (ERA5, sastrugi detected by satellite, sastrugi measured on the field), whereas the EAIIST shows a general agreement between the various datasets. This difference could be attributed to the higher variability of the katabatic wind direction at It-

ITASE; in fact, this site is at the northern limit of megadune field (Fig. 1), and a relatively high variability of katabatic wind direction (>10-15°) could be one of the threshold factor that does not allow the formation of megadune on the northern part. However, with the aim of applying this methodology at large-scale using ERA5 data, e.g., the whole continent, the differences between the two sources can be significant (e.g., at the It-ITASE site), and could produce errors in the SPWD calculation. Therefore, the use of sastrugi could be a more accurate way to interpret prevalent wind direction with high wind speed (≥ 11 m s^{-1}) compared to ERA5.

The SPWD is the only parameter that could be considered as almost constant at 10s km scale, in consideration of the stability of the direction of the katabatic wind, driven mainly by surface slope and the Coriolis force. In contrast, ~~SPWD at km scale,~~ albedo and thermal brightness temperature continuously change annually and during seasons. In fact, NIR albedo significantly varies because of surface changes up to 0.1 α and between the beginning, the middle and end of the summer season ~~(and also changes though the season~~ in relation to the SZA by ± 0.01-0.02~~), while~~ α. Frezzotti et al., (2002b) pointed out the presence of severe sastrugi (up to 1.5 m in height) located on the windward flank and alternation of sastrugi (up to 40 cm) and glazed surfaces are located at the bottom of the interdune area. The observed change on NIR albedo and brightness temperature on the windward flank is correlated to the sastrugi formation and deterioration during the season, and their relative change in shadow (Warren, 1982). While thermal brightness temperature varies from a higher temperature near the summer solstice to lower values in late spring and summer, in the range ± 5-10~~°~~.°K. In both cases, the differences between leeward ~~(~~where glazed surfaces are located) and windward flanks of megadunes are not high enough to overcome the seasonal variability and thus a constant range for albedo and temperature is impossible to determine. Therefore, different models in function of the season (beginning, middle and end) would be necessary to properly detect the two sides of each megadune using automatic methods. However, a near-constant difference between leeward and windward flanks was observed regardless of absolute values. ~~In detail, NIR albedo is on average lower on the leeward flank by 0.04, while broadband albedo by 0.02.~~

4.~~3~~2 Megadune upwind migration

~~The MEaSUREs Programme provides ice motion based on synthetic-aperture radar (SAR) interferometry from multiple satellite systems. The SAR image phase centre penetrates up to 10 m on dry and cold firn (Rignot et al., 2001) and provides information on ice flow and not of surface features. In contrast, using feature tracking on optical images (Landsat and Sentinel 2), it is possible to estimate the absolute migration (migration + ice flow) of surface features. The MEaSUREs ice flow velocity at the D6 site (2.2±1.1 m a^{-1}) is in agreement with the GPS measurement of 1.46 ±0.04 m a^{-1} (Vittuari et al., 2004). MEaSUREs data shows an ice flow of 6.1±3.4 m a^{-1} (52°) for the EAIIST site. As concerns the absolute migration derived from optical images, we calculated a weighted velocity based on the number of calculated features for Landsat, obtaining 13.4±3.6 m a^{-1} (It-ITASE) and 12.6±3.5 m a^{-1} (EAIIST). Applying Eq. (5), we obtained a sedimentological migration of 18.6 m a^{-1} (225°) at EAIIST and 15.5 m a^{-1} (239°) at It-ITASE using Landsat 8 OLI data, and 16.5 m a^{-1} (224°) at EAIIST and 13.6 m a^{-1} (239°) at It-ITASE with Sentinel-2. On the other hand, for the transect at the D6 site, we estimated a sedimentological migration of 11~~

~~m a^{-1} from the comparison of DEMs from GPS (1999) and REMA (2014). GPS and GPR profiles along the It-ITASE traverse show the presence of paleo-megadunes buried under the leeward surface of the megadune field (Frezzotti et al., 2002b). Analysis of the D6 firn core allowed to detect the Tambora eruption signal (1816 AD) at 15.36 m depth with an average snow accumulation of 36±1.8 mm we a^{-1} (Frezzotti et al., 2005). Using the isochrone distance of 1.5-1.8 km between the 180 years old paleo-crest and the recent crest from GPS observations (1998-99 AD), we can evaluate the windward migration of the megadune crest at about 8-10 m a^{-1}. These field results scalarly summed with an ice flow from GPS of 1.46 ±0.04 m a^{-1} with a direction of 97° produced an absolute migration of 10.3 m a^{-1} (214°). Therefore, focusing on the It-ITASE site where both remote data and GPS in situ measurements are present, we found good agreement between the satellite and ground measurement datasets, especially with migration calculated from Sentinel-2 images, which in addition shows a significant lower annual error compared to Landsat (1.7 vs 2.6 m a^{-1}, Table 1). In fact, the calculated sedimentological migration using Sentinel-2 was 13.6 m a^{-1}, very similar to the one obtained from field observations (11 m a^{-1}). In addition, the absolute migration from in situ data (10.3 m a^{-1}) is very close to the one calculated using *IMCORR* on Sentinel-2 imagery (11.5 m a^{-1}). Hence, we observe a general overestimation of sedimentological and absolute migration using remote-sensing with a mean difference of +1.9 m a^{-1} (uncertainties of 19% for sedimentological migration and 10% for absolute migration). Using Landsat images, larger differences were found, with an average overestimation of 3.8 m a^{-1}. This difference could be caused by the fact that with remote sensing a much wider area is included, as opposed to in situ observations which were acquired in transects on a limited section of the megadune field. Further still, the data were obtained at different time periods. Finally, the spatial resolution and geolocation (Mouginot et al., 2017) could affect the satellite data, as demonstrated in the worse results obtained using Landsat images at 15 m spatial resolution against 10 m of Sentinel. Thus, commercial images of high resolution (≈ 1 m or less) might increase the quality of the calculated results, leading to closer agreement to field observations.~~

~~In general, even if the directions between sedimentological migration and ice movement are almost opposite (≈SW and ≈E respectively), it is evident that the sedimentological process has a more relevant effect on megadune migration, by an order of magnitude compared to the influence of ice-flow. Sedimentological processes~~ The absolute position of the megadune crest and trough are driven mainly by two processes: snow ablation/accumulation processes and ice sheet surface flow. GPS and GPR profiles along the It-ITASE traverse show the presence of paleo-megadunes buried up to the investigation depth of 20 m (Frezzotti et al., 2002b). Analysis of the D6 firn core allowed to detect the Tambora eruption signal (1816 AD) at 15.36 m depth with an average snow accumulation of 36±1.8 mm w.e. a^{-1}, whereas an average value of 29±7 mm w.e. a^{-1} of spatial variability in SMB at D6 site was evaluated by GPR calibrated using accumulation at three firn cores (Frezzotti et al., 2005). The elevation change during 15 years observed using GPS and REMA shows a relative increase of accumulation on the windward flank with the maximum value at the trough compared to the glazed surface area from 29 to 46 mm w.e. a^{-1} with an average value of 34 mm w.e. a^{-1}, using a density of 360 kg m^{3} in the first two metres. This value is very close to the estimated change of accumulation in the megadune area from 7 to 35 mm w.e. a^{-1} provided by Frezzotti et al., (2002b) using the variability of GPR internal layering at the megadune site (Fig. 5). The minimum value represents a decrease in accumulation up to 75% or more on glazed surfaces. The relative stability of glazed surfaces with respect to elevation change and NIR albedo confirms

the extremely stable SMB low value of the glazed surfaces with respect to accumulation area, due to the long-term hiatus in SMB forced by wind scouring processes.

Using the isochrone distance of 1.5-1.8 km between the 180 years old paleo-crest detected by GPR and the recent crest from GPS observations (1998-99 AD), we can evaluate the windward migration of the paleo megadune crest at about 8-10 m a^{-1}. This vector from field observations summed with an ice flow from GPS of 1.46 ±0.04 m a^{-1} with a direction of 97° produced an absolute migration of 10.3 m a^{-1} with a direction of 214°. This value is in very good agreement with absolute migration calculated using the elevation comparison between GPS and REMA (11±5.2 m a^{-1}) and with satellite tracking (from 11.4 to 14.0 m a^{-1}), in particular with Sentinel-2 images (11.4 m a^{-1}, Table 1). At the D6 site, the movement components show different intensity with an order of magnitude of difference: 1-2 m a^{-1} for ice flow, versus 13.6-15.4 m a^{-1} for sedimentological migration. The components present nearly opposite directions: 97° for ice flow and 245° for sedimentological migration. The results allowed us to calculate all the components of migration and to conclude that for a megadune with a wavelength of 3 km we could calculate an absolute migration of approximately 10 m a^{-1}. This burying process of snow on glazed surfaces takes about 300 years, with overlap of crest to through and glazed to sastrugi surface as observed by GPR internal layering (Fig. 5).

The megadune migration on the upwind part observed by elevation change and tracking is also confirmed by the comparison of NIR and brightness temperature along the studied transects. These parameters remain relatively stable during the observed time on the glazed surface on the leeward flank, whereas the positive SMB upwind flank and bottom through area changes significantly at pluriannual scale, but also at seasonal scale. Hence, we observe a general overestimation of sedimentological and absolute migration using remote sensing with a mean difference of +1.9 m a^{-1} for Sentinel-2 (uncertainties of 19% for sedimentological migration and 10% for absolute migration). Using Landsat 8 OLI images, larger differences were found, with an average overestimation of 3.8 m a^{-1}. This difference could be caused by spatial variability of processes; with remote sensing we analysed a much wider area, as opposed to in situ observations which were acquired in transects on a limited section of the megadune field. Finally, the spatial resolution and geolocation (Mouginot et al., 2017) could affect the satellite data, as demonstrated by the worse results obtained using Landsat images at 15 m spatial resolution against 10 m of Sentinel-2.

The ice velocity of MEaSUREs is based on SAR images and is in perfect agreement with GPS measurement, and the tracking methods of IMCORR using optical images and crest displacement is in agreement with the migration of morphologies observed from the comparison between change in elevation by GPS and REMA. On the basis of our analysis, the sedimentological processes are analogous at It-ITASE and EAIIST sites. At the second site, a "faster" ice-flow motion was observed by MEaSURE, and the velocity of absolute migration is reduced by almost 3635%, compared to the initial sedimentological-migration velocity.

~~Comparison between the elevation profile from It-ITASE measurements and REMA, 15 years apart, clearly shows the upwind migration of the crest and trough with migration and burying of snow sastrugi over the glazed surface. The glazed surface remains stable in elevation, while the snow-covered surface changes elevation, with a higher accumulation in correspondence with the previous trough, decreasing from the trough towards the windward crest.~~

The ice velocity based on SAR images presents a phase centre that penetrates up to 10 m on dry and cold firn (Rignot et al., 2001) and provides information on ice flow and not surface features. In contrast, using feature tracking on optical images (Landsat and Sentinel-2), it is possible to estimate the absolute migration (migration + ice flow) of surface features that could be significantly different from ice flow as for the megadunes.

5 Conclusions

This study provides new information about the peculiar interaction between atmosphere and cryosphere that drives the megadune formation and evolution. The snow accumulation distribution/variability processes that allow megadune formation have important consequences concerning the choice of sites for ice coring and SMB evaluation, since orographic variations of few metres per kilometre have a significant impact on the snow accumulation process. Furthermore, these new results represent a new ground truth and foundation of knowledge for ice sheet mass balance research, in particular for satellite altimeter and ice velocity derived by remote sensing measurements (e.g., radar vs optical/lidar).

The present study significantly improved the previous knowledge on Antarctic ~~megadunes, confirming previous hypothesis and providing~~megadune temporal/spatial variability and quantified the sedimentation/migration processes and their interaction with atmosphere and ice sheet surface. The results confirm previous hypotheses and provide new relevant information on different aspects of these peculiar landforms~~. We used recent satellite imagery and applied remote sensing methods in conjunction with field data to investigated in detail two areas on the Antarctic plateau, involved in past international and Italian traverses, respectively EAIIST and It-ITASE. Using the highest resolution and most recent DEM of Antarctica, i.e., REMA DEM, we produced aspect and slope maps of these areas, and combining these data with wind direction, we calculated the slope in the prevailing wind direction (SPWD). In fact, SPWD~~ showing that the megadune is a ~~crucial~~dynamic feature ~~in megadune research and, as pointed out in our results, it has strong correlations with other parameters, i.e. albedo and brightness temperature. In order to obtain wind properties, we used climatic reanalysis data from ERA5, validated against wind direction based on sastrugi, local landforms parallel to katabatic wind flows. Then, starting from Landsat 8 OLI imagery, a first numerical optical analysis of megadunes and in particular of their leeward flanks, covered in glazed surfaces, was carried out, calculating albedo (both broadband and NIR) and brightness temperature. In detail, we discovered that~~ at different spatial and temporal scales.

In detail, the leeward glazed flanks show a lower NIR albedo (~~by~~up to 0.~~02~~1) and higher brightness temperatures (up to 1.5 K) compared to windward snow–covered sides~~; the difference in albedo is even higher (i.e. 0.04) in~~ within each of the 5 transects analysed. NIR ~~wavelengths. Albedo~~albedo and thermal brightness temperature, combined with the SPWD, allowed us to produce a ~~detailed and preliminary analysis in time of the extent of~~method for automatically detecting glazed surfaces~~, both intra- and inter-annually. A higher correlation was observed~~. High correlations were found between SPWD and NIR albedo ~~compared to broadband albedo, with an almost doubled correlation coefficient. However, the best agreement is found in the correlation~~and thermal brightness temperature with a R^2 up to 0.44 and 0.57 respectively calculated along the whole transect

examined in 2013-14, with differences between spring and end of summer. The correlations between SPWD and ~~brightness temperature, in particular with Landsat 8 OLI thermal band 10. We found a general areal reduction of glazed surface through the summer season, with~~ NIR albedo on the ~~maximum at the beginning of the summer and the minimum at the end (~~transects decrease ~~of -16%). Conversely, inter-annually we observed an areal increase of such surfaces by at maximum 1% in six years. As these features have a near-zero or negative SMB, they deserve major attention and detailed analysis at higher spatial and time scales. Finally, we provided an analysis~~to 0.39 in comparison with the image from Dec 2019. Moreover, the high correlation of NIR albedo between images decreases over time by up to 60% between Nov 2013 and Dec 2019. Our results show that on wide areas, a large overestimation in the detection of snow glazed surfaces (up to 88%) can result when using only NIR albedo and thermal brightness temperature in the classification, while including the SPWD substantially improves the classification results. However, when applied in narrower areas, where a higher homogeneity of NIR and TIRS1 bands is present, the inclusion of the SPWD is not so relevant, considering also the low availability of high-resolution wind and topographic slope data at different temporal periods, which need to be sufficiently synchronous with spectral imagery, in consideration of the migration of megadunes. Further research might consider other parameters to automatically detect snow glazed surfaces, including snow grain size or the normalised difference snow index.

Finally, we provided for the first time an estimation of megadune migration from field and remote observations~~. As~~ at the It-ITASE site. The results obtained using field ~~data, we used GPS~~ measurements ~~from the It-ITASE traverse~~ and ~~as~~ remote observations ~~and calculated~~allow to calculate all the components of megadune migration, ~~i.e.,~~ absolute ~~and~~(11-14 m a^{-1}), sedimentological migration (13-15 m a^{-1}) and the ice flow~~. We found good agreement between field and satellite measurements, with an overestimation of absolute migration from satellite data of 10% (which, however, considered a different and more recent period). In fact, from field-based observations we obtained a velocity of 10.3 m a^{-1}, compared to 11.5 m a^{-1} with Sentinel~~ (1-2~~. Nevertheless, as Landsat 8 OLI showed worse results than Sentinel-2, having a lower spatial resolution, probably a future implementation of commercial high-resolution satellite imagery would increase the quality of these results. In this context we can~~ m a^{-1}) and to conclude that~~, since~~ for a megadunes ~~have an average~~with a wavelength of 3 km and ~~migrate~~migration of approximately ~~at~~ 10 m a^{-1}, the burying process of snow on glazed surfaces takes about 300 years~~ and this morphogenetic process decreases the albedo of the dune, NIR and broadband, by 0.04 and 0.02 respectively in such period. In the end, our work points out the importance of sedimentological processes in megadune fields with an "opposite direction" between the migration of surface features and ice flow derived respectively from feature tracking of optical images and SAR.~~, with overlap of crest to through and glazed to sastrugi surface. The reconstruction of paleoclimate based on firn/ice cores drilled in megadune areas or downstream is very complex. In megadune areas, the distortion of recordings is ~~characterized~~characterised by a snow accumulation/hiatus periodicity of about hundreds of years. The length of periodic variations due to mesoscale relief and/or megadunes depends on ice velocity, megadune migration and snow accumulation, and can therefore vary in space and time~~. Our results confirm~~ within the ~~already hypothesized upwind migration~~500,000 km^2 of megadune field. In the ~~windward flanks~~end, our work points out the importance of ~~megadunes, validating their~~ "antidunal" ~~formation, finding a relative stability in~~sedimentological processes in megadune fields with an almost opposite direction between the migration of surface features

and ice flow derived respectively from feature tracking of optical images and SAR. These results present significant implication for surface measurements using Radar/Lidar altimetric satellite and measurements of ice flow using optical and SAR image in the megadune area. Moreover, our results point out the different elevation ~~of their leeward face and upward migration of the crest at ten meters per year.~~behaviour at pluriannual scale of the stable elevation and NIR albedo of glazed surface, while the snow-covered surface changes elevation and NIR albedo, with a higher accumulation/elevation in correspondence with the previous trough, decreasing from the trough towards the windward crest. Wind-driven process greatly affects the SMB of the megadune area that imply all or most of the regional accumulation (as determined by RACMO and other models) is gathered in the accretionary faces whereas the downwind area the SMB is near zero with long hiatus in snow accumulation.

Data availability

Data used to the aims of the present study are available upon request to the corresponding ~~author~~authors.

Author contributions

GT, MF conceived the idea of this work. GT and DF developed the procedure and processed the satellite image and data. All authors contributed to the writing of the final manuscript.

Competing interests

The authors declare that they have no conflict of interest.

Acknowledgments

The authors are thankful to MNA–National Antarctic Museum–of Italy (PhD Scholarship of G. Traversa), the Department for Regional Affairs and Autonomies (DARA) of the Italian Presidency of the Council of Ministers and Levissima Sanpellegrino S.p.A. (post-doc fellowship of D. Fugazza). This study was supported by the EAIIST project (ANR-16-CE01- 0011), the Institut Polaire Français Paul-Emile Victor (IPEV), the National Antarctic Research Program (PNRA), the French Research National Agency (Project). The authors would like to warmly thank all the participants of the It-ITASE and EAIIST traverses for their tremendous field contributions allowing the collection of the crucial in situ measurements used in this study.

References

~~Agosta, C., Amory, C., Kittel, C., Orsi, A., Favier, V., Gallée, H., van den Broeke, M. R., Lenaerts, J. T. M., van Wessem, J. M., van de Berg, W. J., and Fettweis, X.: Estimation of the Antarctic surface mass balance using the regional climate model MAR (1979–2015) and identification of dominant processes, The Cryosphere, 13, 281–296, https://doi.org/10.5194/tc-13-281-2019, 2019.~~

Albert, M., Shuman, C., Courville, Z., Bauer, R., Fahnestock, M., and Scambos, T.: Extreme firn metamorphism: impact of decades of vapor transport on near-surface firn at a low-accumulation glazed site on the East Antarctic plateau, Ann. Glaciol., 39, 73–78, https://doi.org/10.3189/172756404781814041, 2004.

Arcone, S. A., Jacobel, R., and Hamilton, G.: Unconformable stratigraphy in East Antarctica: Part I. Large firn cosets, recrystallized growth, and model evidence for intensified accumulation, J. Glaciol., 58, 240–252, https://doi.org/10.3189/2012JoJ11J044, 2012a.

Arcone, S. A., Jacobel, R., and Hamilton, G.: Unconformable stratigraphy in East Antarctica: Part II. Englacial cosets and recrystallized layers, J. Glaciol., 58, 253–264, https://doi.org/10.3189/2012JoG11J045, 2012b.

Bishop, M. P., Björnsson, H., Haeberli, W., Oerlemans, J., Shroder, J. F., and Tranter, M.: Encyclopedia of snow, ice and glaciers, Springer Science & Business Media, 2011.

Canny, J.: A computational approach to edge detection, IEEE Trans. Pattern Anal. Mach. Intell., 679–698, 1986.

Courville, Z. R., Albert, M. R., Fahnestock, M. A., Cathles, L. M., and Shuman, C. A.: Impacts of an accumulation hiatus on the physical properties of firn at a low-accumulation polar site, J. Geophys. Res., 112, F02030, https://doi.org/10.1029/2005JF000429, 2007.

Dadic, R., Mott, R., Horgan, H. J., and Lehning, M.: Observations, theory, and modeling of the differential accumulation of Antarctic megadunes: ACCUMULATION OF ANTARCTIC MEGADUNES, J. Geophys. Res. Earth Surf., 118, 2343–2353, https://doi.org/10.1002/2013JF002844, 2013.

Das, I., Bell, R. E., Scambos, T. A., Wolovick, M., Creyts, T. T., Studinger, M., Frearson, N., Nicolas, J. P., Lenaerts, J. T. M., and van den Broeke, M. R.: Influence of persistent wind scour on the surface mass balance of Antarctica, Nat. Geosci., 6, 367–371, https://doi.org/10.1038/ngeo1766, 2013.

Ekaykin, A. A., Lipenkov, V. Ya., and Shibaev, Yu. A.: Spatial Distribution of the Snow Accumulation Rate Along the Ice Flow Lines Between Ridge B and Lake Vostok, Ice Snow, 52, 122, https://doi.org/10.15356/2076-6734-2012-4-122-128, 2015.

Fahnestock, M. A., Scambos, T. A., and Bindschadler, R. A.: Semi-automated ice velocity determination from satellite imagery, Eos, 73, 493, 1992.

Fahnestock, M. A., Scambos, T. A., Shuman, C. A., Arthern, R. J., Winebrenner, D. P., and Kwok, R.: Snow megadune fields on the East Antarctic Plateau: Extreme atmosphere-ice interaction, Geophys. Res. Lett., 27, 3719–3722, https://doi.org/10.1029/1999GL011248, 2000.

Foga, S., Scaramuzza, P. L., Guo, S., Zhu, Z., Dilley Jr, R. D., Beckmann, T., Schmidt, G. L., Dwyer, J. L., Hughes, M. J., and Laue, B.: Cloud detection algorithm comparison and validation for operational Landsat data products, Remote Sens. Environ., 194, 379–390, https://doi.org/10.1016/j.rse.2017.03.026, 2017.

Frezzotti, M., Gandolfi, S., Marca, F. L., and Urbini, S.: Snow dunes and glazed surfaces in Antarctica: new field and remote-sensing data, Ann. Glaciol., 34, 81–88, https://doi.org/10.3189/172756402781817851, 2002a.

Frezzotti, M., Gandolfi, S., and Urbini, S.: Snow megadunes in Antarctica: Sedimentary structure and genesis, J. Geophys. Res. Atmospheres, 107, ACL 1-1–ACL 1-12, https://doi.org/10.1029/2001JD000673, 2002b.

Frezzotti, M., Pourchet, M., Flora, O., Gandolfi, S., Gay, M., Urbini, S., Vincent, C., Becagli, S., Gragnani, R., and Proposito, M.: New estimations of precipitation and surface sublimation in East Antarctica from snow accumulation measurements, Clim. Dyn., 23, 803–813, https://doi.org/10.1007/s00382-004-0462-5, 2004.

Frezzotti, M., Pourchet, M., Flora, O., Gandolfi, S., Gay, M., Urbini, S., Vincent, C., Becagli, S., Gragnani, R., and Proposito, M.: Spatial and temporal variability of snow accumulation in East Antarctica from traverse data, J. Glaciol., 51, 113–124, https://doi.org/10.3189/172756505781829502, 2005.

Fugazza, D., Senese, A., Azzoni, R. S., Maugeri, M., and Diolaiuti, G. A.: Spatial distribution of surface albedo at the Forni Glacier (Stelvio National Park, Central Italian Alps), Cold Reg. Sci. Technol., 125, 128–137, https://doi.org/10.1016/j.coldregions.2016.02.006, 2016.

Fujii, Y., Yamanouchi, T., Suzuki, K., and Tanaka, S.: Comparison of the Surface Conditions of the Inland Ice Sheet, Dronning Maud Land, Antarctica, Derived from Noaa AVHRR Data with Ground Observation, Ann. Glaciol., 9, 72–75, https://doi.org/10.3189/S0260305500000410, 1987.

Hersbach, H., Bell, B., Berrisford, P., Hirahara, S., Horányi, A., Muñoz-Sabater, J., Nicolas, J., Peubey, C., Radu, R., Schepers, D., Simmons, A., Soci, C., Abdalla, S., Abellan, X., Balsamo, G., Bechtold, P., Biavati, G., Bidlot, J., Bonavita, M., Chiara, G., Dahlgren, P., Dee, D., Diamantakis, M., Dragani, R., Flemming, J., Forbes, R., Fuentes, M., Geer, A., Haimberger, L., Healy, S., Hogan, R. J., Hólm, E., Janisková, M., Keeley, S., Laloyaux, P., Lopez, P., Lupu, C., Radnoti, G., Rosnay, P., Rozum, I., Vamborg, F., Villaume, S., and Thépaut, J.: The ERA5 Global Reanalysis, Q. J. R. Meteorol. Soc., qj.3803, https://doi.org/10.1002/qj.3803, 2020.

Howat, I. M., Porter, C., Smith, B. E., Noh, M.-J., and Morin, P.: The Reference Elevation Model of Antarctica, The Cryosphere, 13, 665–674, https://doi.org/10.5194/tc-13-665-2019, 2019.

Jawak, S. D., Kumar, S., Luis, A. J., Bartanwala, M., Tummala, S., and Pandey, A. C.: Evaluation of geospatial tools for generating accurate glacier velocity maps from optical remote sensing data, in: Multidisciplinary Digital Publishing Institute Proceedings, 341, https://doi.org/10.3390/ecrs-2-05154, 2018.

Jeong, S. and Howat, I. M.: Performance of Landsat 8 Operational Land Imager for mapping ice sheet velocity, Remote Sens. Environ., 170, 90–101, https://doi.org/10.1016/j.rse.2015.08.023, 2015.

Jezek, K. C.: Glaciological properties of the Antarctic ice sheet from RADARSAT-1 synthetic aperture radar imagery, Ann. Glaciol., 29, 286–290, https://doi.org/10.3189/172756499781820969, 1999.

Klok, E. L., Greuell, W., and Oerlemans, J.: Temporal and spatial variation of the surface albedo of Morteratschgletscher, Switzerland, as derived from 12 Landsat images, J. Glaciol., 49, 491–502, https://doi.org/10.3189/172756503781830395, 2003.

Kodama, Y., Wendler, G., and Gosink, J.: The effect of blowing snow on katabatic winds in Antarctica, Ann. Glaciol., 6, 59–62, https://doi.org/10.3189/1985AoG6-1-59-62, 1985.

Liang, S.: Narrowband to broadband conversions of land surface albedo I: Algorithms, Remote Sens. Environ., 76, 213–238, https://doi.org/10.1016/S0034-4257(00)00205-4, 2001.

Mather, K. B.: Further observations on sastrugi, snow dunes and the pattern of surface winds in Antarctica, Polar Rec., 11, 158–171, https://doi.org/10.1017/S0032247400052888, 1962.

Mayewski, P. and Goodwin, I.: Antarctic's role pursued in global climate change, Eos Trans. Am. Geophys. Union, 80, 398–400, https://doi.org/10.1029/EO080i035p00398, 1999.

Meredith, M., Sommerkorn, M., Cassotta, S., Derksen, C., Ekaykin, A., Hollowed, A., Kofinas, G., Mackintosh, A., Melbourne-Thomas, J., and Muelbert, M. M. C.: Polar Regions. Chapter 3, IPCC Special Report on the Ocean and Cryosphere in a Changing Climate, 2019.

Mouginot, J., Rignot, E., Scheuchl, B., and Millan, R.: Comprehensive annual ice sheet velocity mapping using Landsat-8, Sentinel-1, and RADARSAT-2 data, Remote Sens., 9, 364, https://doi.org/10.3390/rs9040364, 2017.

Núñez-González, F. and Martín-Vide, J. P.: Analysis of antidune migration direction, J. Geophys. Res. Earth Surf., 116, https://doi.org/10.1029/2010JF001761, 2011.

Palm, S. P., Yang, Y., Spinhirne, J. D., and Marshak, A.: Satellite remote sensing of blowing snow properties over Antarctica, J. Geophys. Res., 116, D16123, https://doi.org/10.1029/2011JD015828, 2011.

Palm, S. P., Kayetha, V., Yang, Y., and Pauly, R.: Blowing snow sublimation and transport over Antarctica from 11 years of CALIPSO observations, The Cryosphere, 11, 2555–2569, https://doi.org/10.5194/tc-11-2555-2017, 2017.

Parish, T. R. and Bromwich, D. H.: Continental-scale simulation of the Antarctic katabatic wind regime, J. Clim., 4, 135–146, https://doi.org/10.1175/1520-0442(1991)004<0135:CSSOTA>2.0.CO;2, 1991.

Picard, G., Libois, Q., Arnaud, L., Verin, G., and Dumont, M.: Development and calibration of an automatic spectral albedometer to estimate near-surface snow SSA time series, The Cryosphere, 10, 1297–1316, https://doi.org/10.5194/tc-10-1297-2016, 2016.

Pirazzini, R.: Surface albedo measurements over Antarctic sites in summer, J. Geophys. Res., 109, D20118, https://doi.org/10.1029/2004JD004617, 2004.

Proposito, M., Becagli, S., Castellano, E., Flora, O., Genoni, L., Gragnani, R., Stenni, B., Traversi, R., Udisti, R., and Frezzotti, M.: Chemical and isotopic snow variability along the 1998 ITASE traverse from Terra Nova Bay to Dome C, East Antarctica, Ann. Glaciol., 35, 187–194, https://doi.org/10.3189/172756402781817167, 2002.

Prothero, D. R. and Schwab, F.: Sedimentary geology, Macmillan, 2004.

Richards, J. A. and Richards, J. A.: Remote sensing digital image analysis, Springer, 1999.

Rignot, E., Echelmeyer, K., and Krabill, W.: Penetration depth of interferometric synthetic-aperture radar signals in snow and ice, Geophys. Res. Lett., 28, 3501–3504, https://doi.org/10.1029/2000GL012484, 2001.

Rignot, E., Mouginot, J., and Scheuchl, B.: MEaSUREs InSAR-based Antarctica ice velocity map, version 2, Boulder CO NASA DAAC Natl. Snow Ice Data Cent., 2017.

Scambos, T. A., Dutkiewicz, M. J., Wilson, J. C., and Bindschadler, R. A.: Application of image cross-correlation to the measurement of glacier velocity using satellite image data, Remote Sens. Environ., 42, 177–186, 1992.

Scambos, T. A., Frezzotti, M., Haran, T., Bohlander, J., Lenaerts, J. T. M., Van Den Broeke, M. R., Jezek, K., Long, D., Urbini, S., Farness, K., Neumann, T., Albert, M., and Winther, J. G.: Extent of low-accumulation "wind glaze" areas on the East Antarctic plateau: implications for continental ice mass balance, J. Glaciol., 58, 633–647, https://doi.org/10.3189/2012JoG11J232, 2012.

Schaepman-Strub, G., Schaepman, M. E., Painter, T. H., Dangel, S., and Martonchik, J. V.: Reflectance quantities in optical remote sensing—Definitions and case studies, Remote Sens. Environ., 103, 27–42, https://doi.org/10.1016/j.rse.2006.03.002, 2006.

Swithinbank, C.: Antarctica, US Government Printing Office, 1988.

Traversa, G., Fugazza, D., Senese, A., and Diolaiuti, G. A.: Preliminary results on Antarctic albedo from remote sensing observations, Geogr Fis Din Quat, 42, 245–254, http://dx.doi.org/10.4461/GFDQ.2019.42.14, 2019.

Traversa, G., Fugazza, D., and Frezzotti, M.: Analysis of Megadune Fields in Antarctica, in: 2021 IEEE International Geoscience and Remote Sensing Symposium IGARSS, 5513–5516, https://doi.org/10.1109/IGARSS47720.2021.9554827, 2021a.

Traversa, G., Fugazza, D., Senese, A., and Frezzotti, M.: Landsat-8 OLI Broadband Albedo Validation in Antarctica and Greenland, Remote Sens., 13, 799, https://doi.org/10.3390/rs13040799, 2021b.

Van Wessem, J. M., Reijmer, C. H., Morlighem, M., Mouginot, J., Rignot, E., Medley, B., Joughin, I., Wouters, B., Depoorter, M. A., Bamber, J. L., Lenaerts, J. T. M., Van De Berg, W. J., Van Den Broeke, M. R., and Van Meijgaard, E.: Improved representation of East Antarctic surface mass balance in a regional atmospheric climate model, J. Glaciol., 60, 761–770, https://doi.org/10.3189/2014JoG14J051, 2014.

Vermote, E. F., Tanré, D., Deuze, J. L., Herman, M., and Morcette, J. J.: Second simulation of the satellite signal in the solar spectrum, 6S: An overview, IEEE Trans. Geosci. Remote Sens., 35, 675–686, https://doi.org/10.1109/36.581987, 1997.

Vittuari, L., Vincent, C., Frezzotti, M., Mancini, F., Gandolfi, S., Bitelli, G., and Capra, A.: Space geodesy as a tool for measuring ice surface velocity in the Dome C region and along the ITASE traverse, Ann. Glaciol., 39, 402–408, https://doi.org/10.3189/172756404781814627, 2004.

Warren, S. G.: Optical properties of snow, Rev. Geophys., 20, 67–89, https://doi.org/10.1029/RG020i001p00067, 1982.

Watanabe, O.: Distribution of surface features of snow cover in Mizuho Plateau, http://id.nii.ac.jp/1291/00000854/, 1978.

~~Wendler, G., André, J. C., Pettré, P., Gosink, J., and Parish, T.: Katabatic winds in Adélie coast, Antarct. Meteorol. Climatol. Stud. Based Autom. Weather Stn., 61, 23–46, https://doi.org/10.1029/AR061p0023, 1993.~~

~~Zanter, K.: Landsat 8 (L8) data users handbook, Landsat Sci. Off. Website, 2019.~~

Agosta, C., Amory, C., Kittel, C., Orsi, A., Favier, V., Gallée, H., van den Broeke, M. R., Lenaerts, J. T. M., van Wessem, J. M., van de Berg, W. J., and Fettweis, X.: Estimation of the Antarctic surface mass balance using the regional climate model MAR (1979–2015) and identification of dominant processes, The Cryosphere, 13, 281–296, https://doi.org/10.5194/tc-13-281-2019, 2019.

Albert, M., Shuman, C., Courville, Z., Bauer, R., Fahnestock, M., and Scambos, T.: Extreme firn metamorphism: impact of decades of vapor transport on near-surface firn at a low-accumulation glazed site on the East Antarctic plateau, Ann. Glaciol., 39, 73–78, https://doi.org/10.3189/172756404781814041, 2004.

Arcone, S. A., Jacobel, R., and Hamilton, G.: Unconformable stratigraphy in East Antarctica: Part I. Large firn cosets, recrystallized growth, and model evidence for intensified accumulation, J. Glaciol., 58, 240–252, https://doi.org/10.3189/2012JoJ11J044, 2012a.

Arcone, S. A., Jacobel, R., and Hamilton, G.: Unconformable stratigraphy in East Antarctica: Part II. Englacial cosets and recrystallized layers, J. Glaciol., 58, 253–264, https://doi.org/10.3189/2012JoG11J045, 2012b.

Bishop, M. P., Björnsson, H., Haeberli, W., Oerlemans, J., Shroder, J. F., and Tranter, M.: Encyclopedia of snow, ice and glaciers, Springer Science & Business Media, 2011.

Canny, J.: A computational approach to edge detection, IEEE Trans. Pattern Anal. Mach. Intell., 679–698, 1986.

Courville, Z. R., Albert, M. R., Fahnestock, M. A., Cathles, L. M., and Shuman, C. A.: Impacts of an accumulation hiatus on the physical properties of firn at a low-accumulation polar site, J. Geophys. Res., 112, F02030, https://doi.org/10.1029/2005JF000429, 2007.

Dadic, R., Mott, R., Horgan, H. J., and Lehning, M.: Observations, theory, and modeling of the differential accumulation of Antarctic megadunes: ACCUMULATION OF ANTARCTIC MEGADUNES, J. Geophys. Res. Earth Surf., 118, 2343–2353, https://doi.org/10.1002/2013JF002844, 2013.

Das, I., Bell, R. E., Scambos, T. A., Wolovick, M., Creyts, T. T., Studinger, M., Frearson, N., Nicolas, J. P., Lenaerts, J. T. M., and van den Broeke, M. R.: Influence of persistent wind scour on the surface mass balance of Antarctica, Nat. Geosci., 6, 367–371, https://doi.org/10.1038/ngeo1766, 2013.

Ekaykin, A. A., Lipenkov, V. Ya., and Shibaev, Yu. A.: Spatial Distribution of the Snow Accumulation Rate Along the Ice Flow Lines Between Ridge B and Lake Vostok, Ice Snow, 52, 122, https://doi.org/10.15356/2076-6734-2012-4-122-128, 2015.

Fahnestock, M. A., Scambos, T. A., and Bindschadler, R. A.: Semi-automated ice velocity determination from satellite imagery, Eos, 73, 493, 1992.

Fahnestock, M. A., Scambos, T. A., Shuman, C. A., Arthern, R. J., Winebrenner, D. P., and Kwok, R.: Snow megadune fields on the East Antarctic Plateau: Extreme atmosphere-ice interaction, Geophys. Res. Lett., 27, 3719–3722, https://doi.org/10.1029/1999GL011248, 2000.

Foga, S., Scaramuzza, P. L., Guo, S., Zhu, Z., Dilley Jr, R. D., Beckmann, T., Schmidt, G. L., Dwyer, J. L., Hughes, M. J., and Laue, B.: Cloud detection algorithm comparison and validation for operational Landsat data products, Remote Sens. Environ., 194, 379–390, https://doi.org/10.1016/j.rse.2017.03.026, 2017.

Frezzotti, M., Gandolfi, S., Marca, F. L., and Urbini, S.: Snow dunes and glazed surfaces in Antarctica: new field and remote-sensing data, Ann. Glaciol., 34, 81–88, https://doi.org/10.3189/172756402781817851, 2002a.

Frezzotti, M., Gandolfi, S., and Urbini, S.: Snow megadunes in Antarctica: Sedimentary structure and genesis, J. Geophys. Res. Atmospheres, 107, ACL 1-1-ACL 1-12, https://doi.org/10.1029/2001JD000673, 2002b.

Frezzotti, M., Pourchet, M., Flora, O., Gandolfi, S., Gay, M., Urbini, S., Vincent, C., Becagli, S., Gragnani, R., and Proposito, M.: New estimations of precipitation and surface sublimation in East Antarctica from snow accumulation measurements, Clim. Dyn., 23, 803–813, https://doi.org/10.1007/s00382-004-0462-5, 2004.

Frezzotti, M., Pourchet, M., Flora, O., Gandolfi, S., Gay, M., Urbini, S., Vincent, C., Becagli, S., Gragnani, R., and Proposito, M.: Spatial and temporal variability of snow accumulation in East Antarctica from traverse data, J. Glaciol., 51, 113–124, https://doi.org/10.3189/172756505781829502, 2005.

Fugazza, D., Senese, A., Azzoni, R. S., Maugeri, M., and Diolaiuti, G. A.: Spatial distribution of surface albedo at the Forni Glacier (Stelvio National Park, Central Italian Alps), Cold Reg. Sci. Technol., 125, 128–137, https://doi.org/10.1016/j.coldregions.2016.02.006, 2016.

Fujii, Y., Yamanouchi, T., Suzuki, K., and Tanaka, S.: Comparison of the Surface Conditions of the Inland Ice Sheet, Dronning Maud Land. Antarctica. Derived from Noaa AVHRR Data with Ground Observation, Ann. Glaciol., 9, 72–75, https://doi.org/10.3189/S0260305500000410, 1987.

Gallet, J. C., Domine, F., Savarino, J., Dumont, M., & Brun, E.: The growth of sublimation crystals and surface hoar on the Antarctic plateau, The Cryosphere, 8(4), 1205-1215, 2014.

Hersbach, H., Bell, B., Berrisford, P., Hirahara, S., Horányi, A., Muñoz-Sabater, J., Nicolas, J., Peubey, C., Radu, R., Schepers, D., Simmons, A., Soci, C., Abdalla, S., Abellan, X., Balsamo, G., Bechtold, P., Biavati, G., Bidlot, J., Bonavita, M., Chiara, G., Dahlgren, P., Dee, D., Diamantakis, M., Dragani, R., Flemming, J., Forbes, R., Fuentes, M., Geer, A., Haimberger, L., Healy, S., Hogan, R. J., Hólm, E., Janisková, M., Keeley, S., Laloyaux, P., Lopez, P., Lupu, C., Radnoti, G., Rosnay, P., Rozum, I., Vamborg, F., Villaume, S., and Thépaut, J.: The ERA5 Global Reanalysis, Q. J. R. Meteorol. Soc., qj.3803, https://doi.org/10.1002/qj.3803, 2020.

Howat, I. M., Porter, C., Smith, B. E., Noh, M.-J., and Morin, P.: The Reference Elevation Model of Antarctica, The Cryosphere, 13, 665–674, https://doi.org/10.5194/tc-13-665-2019, 2019.

Jawak, S. D., Kumar, S., Luis, A. J., Bartanwala, M., Tummala, S., and Pandey, A. C.: Evaluation of geospatial tools for generating accurate glacier velocity maps from optical remote sensing data, in: Multidisciplinary Digital Publishing Institute Proceedings, 341, https://doi.org/10.3390/ecrs-2-05154, 2018.

Jezek, K. C.: Glaciological properties of the Antarctic ice sheet from RADARSAT-1 synthetic aperture radar imagery, Ann. Glaciol., 29, 286–290, https://doi.org/10.3189/172756499781820969, 1999.

Klok, E. L., Greuell, W., and Oerlemans, J.: Temporal and spatial variation of the surface albedo of Morteratschgletscher, Switzerland, as derived from 12 Landsat images, J. Glaciol., 49, 491–502, https://doi.org/10.3189/172756503781830395, 2003.

Kodama, Y., Wendler, G., and Gosink, J.: The effect of blowing snow on katabatic winds in Antarctica, Ann. Glaciol., 6, 59–62, https://doi.org/10.3189/1985AoG6-1-59-62, 1985.

Liang, S.: Narrowband to broadband conversions of land surface albedo I: Algorithms, Remote Sens. Environ., 76, 213–238, https://doi.org/10.1016/S0034-4257(00)00205-4, 2001.

Mather, K. B.: Further observations on sastrugi, snow dunes and the pattern of surface winds in Antarctica, Polar Rec., 11, 158–171, https://doi.org/10.1017/S0032247400052888, 1962.

Mayewski, P. and Goodwin, I.: Antarctic's role pursued in global climate change, Eos Trans. Am. Geophys. Union, 80, 398–400, https://doi.org/10.1029/EO080i035p00398, 1999.

Meredith, M., Sommerkorn, M., Cassotta, S., Derksen, C., Ekaykin, A., Hollowed, A., Kofinas, G., Mackintosh, A., Melbourne-Thomas, J., and Muelbert, M. M. C.: Polar Regions. Chapter 3, IPCC Special Report on the Ocean and Cryosphere in a Changing Climate, 2019.

Mouginot, J., Rignot, E., Scheuchl, B., and Millan, R.: Comprehensive annual ice sheet velocity mapping using Landsat-8, Sentinel-1, and RADARSAT-2 data, Remote Sens., 9, 364, https://doi.org/10.3390/rs9040364, 2017.

Núñez-González, F. and Martín-Vide, J. P.: Analysis of antidune migration direction, J. Geophys. Res. Earth Surf., 116, https://doi.org/10.1029/2010JF001761, 2011.

Palm, S. P., Yang, Y., Spinhirne, J. D., and Marshak, A.: Satellite remote sensing of blowing snow properties over Antarctica, J. Geophys. Res., 116, D16123, https://doi.org/10.1029/2011JD015828, 2011.

Palm, S. P., Kayetha, V., Yang, Y., and Pauly, R.: Blowing snow sublimation and transport over Antarctica from 11 years of CALIPSO observations, The Cryosphere, 11, 2555–2569, https://doi.org/10.5194/tc-11-2555-2017, 2017.

Parish, T. R. and Bromwich, D. H.: Continental-scale simulation of the Antarctic katabatic wind regime, J. Clim., 4, 135–146, https://doi.org/10.1175/1520-0442(1991)004<0135:CSSOTA>2.0.CO;2, 1991.

Picard, G., Libois, Q., Arnaud, L., Verin, G., and Dumont, M.: Development and calibration of an automatic spectral albedometer to estimate near-surface snow SSA time series, The Cryosphere, 10, 1297–1316, https://doi.org/10.5194/tc-10-1297-2016, 2016.

Pietroni, I., Argentini, S., & Petenko, I.. One year of surface-based temperature inversions at Dome C, Antarctica. Boundary-Layer Meteorology, 150(1), 131-151, 2014.

Pirazzini, R.: Surface albedo measurements over Antarctic sites in summer, J. Geophys. Res., 109, D20118, https://doi.org/10.1029/2004JD004617, 2004.

Proposito, M., Becagli, S., Castellano, E., Flora, O., Genoni, L., Gragnani, R., Stenni, B., Traversi, R., Udisti, R., and Frezzotti, M.: Chemical and isotopic snow variability along the 1998 ITASE traverse from Terra Nova Bay to Dome C, East Antarctica, Ann. Glaciol., 35, 187–194, https://doi.org/10.3189/172756402781817167, 2002.

Prothero, D. R. and Schwab, F.: Sedimentary geology, Macmillan, 2004.

Rignot, E., Echelmeyer, K., and Krabill, W.: Penetration depth of interferometric synthetic-aperture radar signals in snow and ice, Geophys. Res. Lett., 28, 3501–3504, https://doi.org/10.1029/2000GL012484, 2001.

Rignot, E., Mouginot, J., and Scheuchl, B.: MEaSUREs InSAR-based Antarctica ice velocity map, version 2, Boulder CO NASA DAAC Natl. Snow Ice Data Cent., 2017.

Scambos, T. A., Dutkiewicz, M. J., Wilson, J. C., and Bindschadler, R. A.: Application of image cross-correlation to the measurement of glacier velocity using satellite image data, Remote Sens. Environ., 42, 177–186, 1992.

Scambos, T. A., Frezzotti, M., Haran, T., Bohlander, J., Lenaerts, J. T. M., Van Den Broeke, M. R., Jezek, K., Long, D., Urbini, S., Farness, K., Neumann, T., Albert, M., and Winther, J.-G.: Extent of low-accumulation "wind glaze" areas on the East Antarctic plateau: implications for continental ice mass balance, J. Glaciol., 58, 633–647, https://doi.org/10.3189/2012JoG11J232, 2012.

Schaepman-Strub, G., Schaepman, M. E., Painter, T. H., Dangel, S., and Martonchik, J. V.: Reflectance quantities in optical remote sensing—Definitions and case studies, Remote Sens. Environ., 103, 27–42, https://doi.org/10.1016/j.rse.2006.03.002, 2006.

Swithinbank, C.: Antarctica, US Government Printing Office, 1988.

Traversa, G., Fugazza, D., Senese, A., and Diolaiuti, G. A.: Preliminary results on Antarctic albedo from remote sensing observations, Geogr Fis Din Quat, 42, 245–254, http://dx.doi.org/10.4461/GFDQ.2019.42.14, 2019.

Traversa, G., Fugazza, D., Senese, A., and Frezzotti, M.: Landsat 8 OLI Broadband Albedo Validation in Antarctica and Greenland, Remote Sens., 13, 799, https://doi.org/10.3390/rs13040799, 2021a.

Traversa, G., Fugazza, D., and Frezzotti, M.: Analysis of Megadune Fields in Antarctica, in: 2021 IEEE International Geoscience and Remote Sensing Symposium IGARSS, 5513–5516, https://doi.org/10.1109/IGARSS47720.2021.9554827, 2021b.

Traversa, G. and Fugazza, D.: Evaluation of Anisotropic Correction Factors for the Calculation of Landsat 8 OLI Albedo on the Ice Sheets, Geogr Fis Din Quar, 44, 91-95, http://dx.doi.org/10.4461/GFDQ.2021.44.8, 2021c.

Van Wessem, J. M., Reijmer, C. H., Morlighem, M., Mouginot, J., Rignot, E., Medley, B., Joughin, I., Wouters, B., Depoorter, M. A., Bamber, J. L., Lenaerts, J. T. M., Van De Berg, W. J., Van Den Broeke, M. R., and Van Meijgaard, E.: Improved representation of East Antarctic surface mass balance in a regional atmospheric climate model, J. Glaciol., 60, 761–770, https://doi.org/10.3189/2014JoG14J051, 2014.

Vermote, E. F., Tanré, D., Deuze, J. L., Herman, M., and Morcette, J.-J.: Second simulation of the satellite signal in the solar spectrum, 6S: An overview, IEEE Trans. Geosci. Remote Sens., 35, 675–686, https://doi.org/10.1109/36.581987, 1997.

Vittuari, L., Vincent, C., Frezzotti, M., Mancini, F., Gandolfi, S., Bitelli, G., and Capra, A.: Space geodesy as a tool for measuring ice surface velocity in the Dome C region and along the ITASE traverse, Ann. Glaciol., 39, 402–408, https://doi.org/10.3189/172756404781814627, 2004.

Warren, S. G.: Optical properties of snow, Rev. Geophys., 20, 67–89, https://doi.org/10.1029/RG020i001p00067, 1982.

Watanabe, O.: Distribution of surface features of snow cover in Mizuho Plateau, http://id.nii.ac.jp/1291/00000854/, 1978.

Wendler, G., André, J. C., Pettré, P., Gosink, J., and Parish, T.: Katabatic winds in Adélie coast, Antarct. Meteorol. Climatol. Stud. Based Autom. Weather Stn., 61, 23–46, https://doi.org/10.1029/AR061p0023, 1993.

Zanter, K.: Landsat 8 (L8) data users handbook, Landsat Sci. Off. Website, 2019.

Appendix A

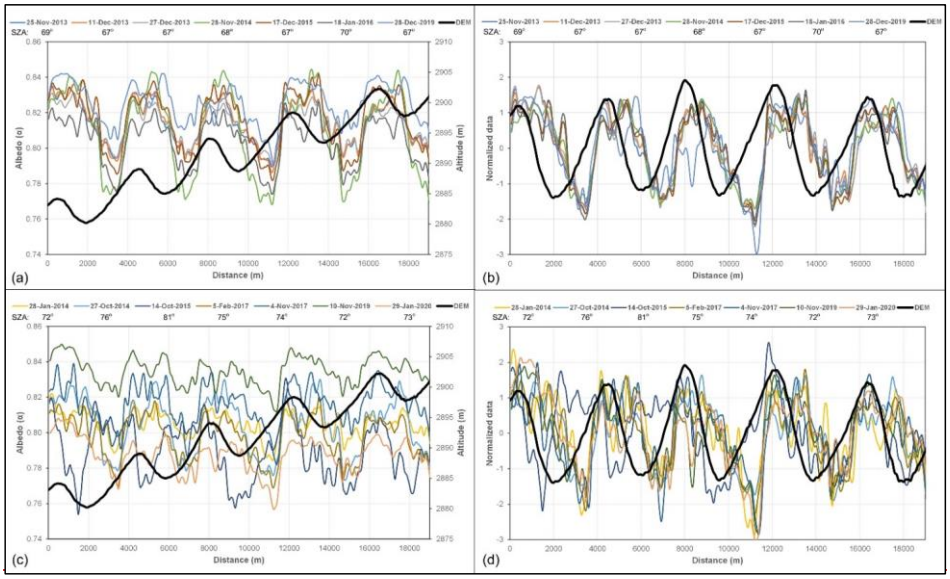

~~**Figure A1: Transect C NIR albedo at the EAIIST site (Fig. 2 for location) for scenes with a SZA < 70° (a) and > 70° (c) with topography. Normalized NIR albedo of scenes with SZA < 70° (b) and > 70° (d) with detrended topography.**~~

Sensor	Tile	Scene	Solar Zenith (deg)	Azimuth (deg)
~~ETM+~~	~~069119~~	~~29-Dec-1999~~	~~67~~	~~95~~
~~ETM+~~	~~081114~~	~~02-Jan-2000~~	~~62~~	~~71~~
OLI	**069119**	**25-Nov-2013**	**69**	**89**
OLI	069119	11-Dec-2013	67	91
OLI	069119	27-Dec-2013	67	93
OLI	069119	28-Jan-2014	72	95
~~OLI~~	~~069119~~	~~27-Oct-2014~~	~~76~~	~~87~~
OLI	**069119**	**28-Nov-2014**	**68**	**89**

~~OLI~~	~~069119~~	~~14-Oct-2015~~	~~81~~	~~87~~
OLI	**069119**	**17-Dec-2015**	**67**	**92**
OLI	069119	18-Jan-2016	70	95
~~OLI~~	~~069119~~	~~05-Feb-2017~~	~~75~~	~~95~~
OLI	**069119**	**04-Nov-2017**	**74**	**87**
OLI	069119	10-Nov-2019	72	88
OLI	069119	28-Dec-2019	67	93
OLI	069119	29-Jan-2020	73	95
OLI	081114	31-Oct-2014	68	62
OLI	081114	02-Dec-2014	61	65
OLI	081114	18-Dec-2014	60	67
OLI	081114	06-Jan-2016	62	69
~~OLI~~	~~081114~~	~~21-Sep-2017~~	~~83~~	~~61~~
OLI	**081114**	**30-Nov-2019**	**62**	**65**
OLI	081114	17-Jan-2020	64	70
S2	T51CWL	10-Jan-2018	67	87
S2	T51CWL	02-Jan-2021	66	84
S2	T52CEA	13-Dec-2016	59	59
S2	T52CEA	27-Dec-2020	59	61

Table A1. Landsat (~~ETM+ and~~ OLI) and Sentinel-2 (S2) images in the EAIIST (069119 and T51CWL tiles for L8OLI and S2, respectively) and It-ITASE (081114 and T52CEA tiles fo L8OLI and S2, respectively) areas used in the study with corresponding Solar Zenith and Azimuth angles from the Landsat/Sentinel Metadata.

Year	It-ITASE		EAIIST	
	Nº of stripes	Percentage of the total	N° of stripes	Percentage of the total
2008	5	0.4 %	5	0.5 %
2009	13	0.9 %	11	1.2 %
2010	27	1.9 %	27	2.9 %
2011	128	9.0 %	44	4.7 %

Celle inserite

Celle inserite

2012	27	1.9 %	16	1.7 %
2013	110	7.7 %	89	9.5 %
2014	217	15.2 %	184	19.6 %
2015	136	9.5 %	61	6.5 %
2016	593	41.6 %	398	42.5 %
2017	169	11.9 %	102	10.9 %

Table A2. Frequency of REMA DEM stripes at the EAIIST and It-ITASE sites from different years, based on the REMA strip index.

EAIIST				**It-ITASE**			
Dataset	**Average**	**Max**	**Min**	**Dataset**	**Average**	**Max**	**Min**
Landsat 8	224°	232°	212°	*Landsat 8*	240°	250°	215°
ERA5 ≥ 0m/s	225°	230°	220°	*ERA5 ≥ 0m/s*	227°	236°	215°
ERA5 ≥ 3m/s	225°	229°	220°	*ERA5 ≥ 3m/s*	226°	233°	217°
ERA5 ≥ 5m/s	225°	229°	220°	*ERA5 ≥ 5m/s*	226°	234°	217°
ERA5 ≥ 7m/s	225°	235°	220°	*ERA5 ≥ 7m/s*	227°	236°	218°
ERA5 ≥11m/s	223°	229°	216°	*ERA5 ≥11m/s*	231°	240°	223°

Table A3. Wind direction statistics (average, maximum and minimum values) for the considered datasets: Landsat 8 at 30 m spatial resolution and ERA5 at 30 km spatial resolution (divided into 5 sub-datasets according to wind speed) at the EAIIST and It-ITASE sites.